Siddharth Iyer

Gas refractometry using hollow core photonic bandgap fiber

School of Electrical Engineering

Thesis submitted for examination for the degree of Master of Science in Technology.

Espoo 9.03.2015

Thesis supervisor:

Hanne Ludvigsen, Docent

Thesis advisor:

Dr. Igor Shavrin

Aalto-yliopisto
Sähkötekniikan korkeakoulu

AALTO UNIVERSITY
SCHOOL OF ELECTRICAL ENGINEERING

ABSTRACT OF THE
MASTER'S THESIS

Author: Siddharth Iyer

Title: Gas refractometry using hollow core photonic bandgap fiber

Date: 9.03.2015 Language: English Number of pages: 6+48

Department of Micro and Nanosciences

Professorship: Micro and Nanotechnology Code: ELEC004Z

Supervisor: Hanne Ludvigsen, Docent

Advisor: Dr. Igor Shavrin

Over the last two decades, much research has been carried out on sensors based on photonic crystal fibers. Their unique structure comprising of a periodic array of air holes running along their length provides optical properties that are highly suited for refractometer sensors.

The thesis presents a fiber-optic interferometric gas refractometer which is capable of spectrally resolved measurements of both real and imaginary parts of the complex refractive index. The refractometer is based on an earlier fiber based Mach-Zehnder-type refractometer design that was used to determine the refractive index of air-acetylene mixture. The aim of the thesis was to improve the device design in order to ascertain the refractive index of pure acetylene. The device adopts a hollow-core photonic bandgap fiber as both a sample cell and a waveguide. This provides the best overlap between probing light and the analyte. In addition, it requires a very small volume of the analyte due to the small dimensions of the fiber, and the sample cell can be made long while keeping the device compact.

The complex refractive index of ∼96% pure acetylene was measured within the optical C band where the gas has a number of pronounced resonance frequencies. The measurement was repeated in ∼500 Pa air and was used as reference for interpreting the results for acetylene. The optical absorption and refractive index change of acetylene over the resonance frequencies were analyzed and its absorption coefficient and refractive index were calculated. The demonstrated capability of this device to measure the real and imaginary parts of the refractive index of an analyte has important implications in the sensor industry.

Keywords: Gas refractometer, hollow core photonic bandgap fiber, Mach-Zehnder interferometer, complex refractive index, fiber sensor.

Acknowledgments

This thesis work has been carried out in the Fiber Optics research group of the Department of Micro- and Nanosciences at Aalto University.

I would like the thank my supervisor Hanne Ludvigsen for giving me the opportunity to work on this exciting project in her group. Her constant guidance was invaluable and her patience as a mentor helped me learn a great deal about sound scientific writing skills and research.

I would also like to express my gratitude to my adviser, Dr. Igor Shavrin. His hands-on expertise, knowledge, and passion for research inspired me and motivated me to keep learning and improving. I am grateful to Sami Kujala as well, who took the time to go through my thesis and suggest improvements.

I would like to thank my colleagues who made working fun, and were there to help me when I got stuck.

Finally, I would like to thank my family for their never-ending support.

Otaniemi, 09.03.2015

Siddharth Iyer

Contents

Symbols and abbreviations

Symbols

v_P	Phase velocity
μ	Magnetic permittivity
ϵ	Electric permittivity
c_0	Speed of light in vacuum
n	Refractive index
κ	Extinction coefficient
α	Absorption coefficient
$\Delta\phi$	Phase difference
L_s	Length of sample arm
L_r	Length of reference arm
θ_i	Angle of incidence
θ_r	Angle of refraction
θ_c	Critical angle
I_s	Intensity in sample arm
I_r	Intensity in reference arm
n_s	Refractive index of the interferometer sample arm
n_r	Refractive index of the interferometer reference arm
n_{eff}	Effective refractive index
$A(\lambda)$	Amplitude of interference fringes at wavelength λ
$T(\lambda)$	Transmission at wavelength λ
λ	Wavelength in free space

Abbreviations

MP	Measuring prism
SMF	Single-mode fiber
PCF	Photonic crystal fiber
HC-PBF	Hollow-core photonic bandgap fiber
RIU	Refractive index unit
OPL	Optical path length
TIR	Total internal reflection
M-TIR	Modified total internal reflection
TEM	Transverse electromagnetic
HCF	Hollow core fiber
DC	Direct current
MI	Modal interference

1 Introduction

A refractometer is a device that enables the measurement of the refractive index of an analyte. A high resolution device is important for the identification of substances, and for measuring their chemical properties such as concentration and composition. The first refractometers were based on critical angle effect, and were capable of determining the concentration of substances [1]. Others based on deflection method were developed next, such as the V - block [2]. Newer devices implemented interferometers into their design and provided higher sensitivity refractive index results. The principle of interferometric refractometers is based on the analysis of interference fringes to explain the properties of an unknown sample introduced into one of the interferometer arms. A change in the refractive index of a sample causes a change in fringe position and amplitude at the interferometer output. By studying these changes, the refractive index of the sample can be accurately measured. Refractometers implementing different interferometer designs such as Fabry-Perot [3–5], Michelson [6–8], and Mach-Zehnder [9] have been developed.

The complete complex refractive index of a material constitutes the wavelength dependent absorption coefficient and the refractive index of that material. Light emitted at resonance wavelengths of a medium undergo high absorption when traveling through it and there is a characteristic refractive index change at those wavelengths. This spectrum is unique for a medium and can be used as an identifier. However, in order to calculate the complex refractive index using an interferometric refractometer, a good overlap between light and the sample is required.

Optical fibers have garnered interest in the sensor industry as they provide the possibility for long light and matter interaction [10, 11]. In addition, they are compact, insensitive to electromagnetic noise, and allow remote and in-situ monitoring of the environment. Gas sensors are required in particularly harsh locations that have extreme heat fluctuations, vibrations, humidity, and corrosive or explosive settings. The integration of optical fibers has made gas sensors more durable in these environments.

The class of photonic crystal fibers, especially hollow core photonic band-gap fibers (HC-PBFs), have emerged as efficient tools for gas sensing. The hollow core can confine light and sample gases simultaneously which provides the best possible over-

lap between both. These fibers can be used in an interferometric setup that allows accurate observation of gas properties by studying the light interaction in the fiber core [12].

The aim of this thesis is to determine the complex refractive index of pure acetylene. The refractometer design applied in this study is one of the first proof of principle devices that uses a photonic bandgap fiber to accurately determine the complex refractive index of a gas. Acetylene gas was used as the test analyte as it has a number of pronounced resonances in the C band where the fiber was designed to operate [13]. The complex refractive index was determined using a HC-PBF based interferometric refractometer. The set-up involves a Mach-Zehnder-type interferometer arrangement using the HC-PBF as the sample arm. The HC-PBF was enclosed at both ends by two evacuated chambers in order to maintain the pressure along the fiber. Acetylene was used as the test analyte, and it was diffused into the HC-PBF through one of the chambers. The measurement was repeated for a reference gas of known refractive index, and this was used to estimate the complex refractive index of acetylene.

The thesis work is divided into six chapters. The principles of refractometry are presented in Chapter 2. The concept of complex refractive index and the significance of its measurement for sensor applications is explained. This is followed by an introduction to interferometry and the working principles of Michelson and Mach-Zehnder interferometers. Since a Mach-Zehnder-type interferometer was chosen for this study, a more in depth discussion of the properties of this interferometer is provided. The physical concepts of optical fibers are discussed and a review of interferometric refractometers based on optical fibers is provided. At the end of the chapter, a brief description of sensor performance parameters such as sensitivity, accuracy, and resolution is provided.

The experimental refractometer is presented in Chapter 3 and the measurement process is explained in detail. In addition, the physical concepts that underlie the refractive index measurement using the model presented in this thesis is discussed. In Chapter 4 the results of our measurements are presented and analyzed. This is followed by a discussion of the methods used and the implications of the results in Chapter 5. The thesis is summarized in Chapter 6.

2 Refractometry

Refractometry is a technique that measures how incident light is affected by a material. The measure of refractive index is specific to a material, and depends on temperature and frequency of the incident light [14]. This allows the determination of a materials composition, concentration, detection and identification [15].

The first refractometer built was the Abbe refractometer. It used the critical angle effect to determine the refractive index of substances. It was proposed by Ernst Abbe in 1869 [16]. It consists of two prisms - one measuring prism and one illuminating prism. The analyte is placed between the two prism plates and light from a diffused source is directed towards the illuminating prism. The design of the refractometer is shown schematically in Fig. 1.

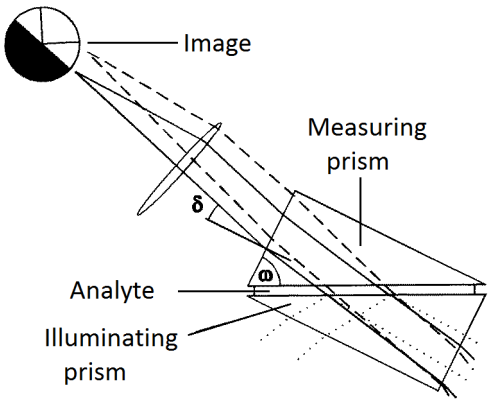

Figure 1: Schematic representation of an Abbe refractometer [17].

The inner side of the illuminating prism is ground so that light scatters in every direction before entering the measuring prism (MP). The refractive index of the MP is higher than that of the analyte, and the incident light entering at grazing angles will be diffracted at critical angle at the bottom. This is seen as a sharp boundary between light and dark sides of the prism system by a telescope. With the known refractive index of the MP, knowing the angle at which the boundary occurs allows the calculation of the critical angle and the refractive index of the analyte using Snell's law [18]. The accuracy of Abbe refractometers is affected by the quality of the contact between the analyte and the prisms and the degree of optical absorption of the analyte. Modern Abbe refractometers achieve a resolution of 1×10^{-4} RIU [19]. RIU stands for refractive index unit and it is the minimum detectable change in the refractive index of an analyte.

A V-block refractometer operates on the deflection method. The test analyte is placed in a V-shaped glass block of known refractive index with perpendicular sides. Collimated light from a source is refracted twice at the two perpendicular block walls,

and the angle of the emerging light beam is dependent on the refractive index of the block and the analyte. The working principle of the device illustrated in Fig. 2.

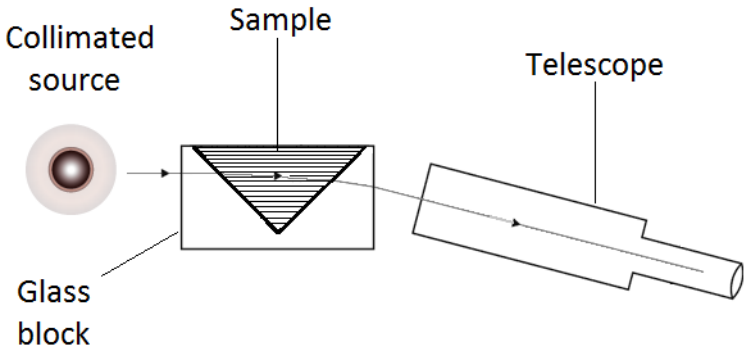

Figure 2: Schematic representation of a V-block refractometer.

Knowing the exit angle and the refractive index of the glass block, the refractive index of the analyte can be calculated. A V-block refractometer has a measurement resolution of 1×10^{-4} RIU [16].

2.1 Complex refractive index

For a dielectric media, there is linear relation between electric field and the induced polarization density

$$P = \epsilon_0 \chi E, \tag{1}$$

where, ϵ_0 is the permittivity of free space, and χ is the electrical susceptibility.

The electrical permittivity of the medium is given by

$$\epsilon = \epsilon_0(1 + \chi). \tag{2}$$

Dielectric materials absorb light at specific frequencies which is dependent on the properties of the media. To take into account the absorption of light, the electrical susceptibility χ takes a complex value

$$\chi = \chi' + j\chi'', \tag{3}$$

which corresponds to the complex permittivity $\epsilon = \epsilon_0(1 + \chi)$. The wavenumber k is dependent on ϵ and becomes complex valued as well

$$k = k_0\sqrt{1 + \chi} = k_0\sqrt{1 + \chi' + j\chi''}. \tag{4}$$

The wavenumber can be written in terms of its real and imaginary parts

$$k = \beta - j\frac{1}{2}\alpha, \tag{5}$$

where α and β are real.

$$\beta - j\frac{1}{2}\alpha = k_0\sqrt{1 + \chi' + j\chi''}. \tag{6}$$

α is the absorption coefficient of the dielectric medium, and β is the propagation constant. The propagation constant is the product of the refractive index and vacuum wavenumber

$$\beta = nk_0. \tag{7}$$

Substituting for β in Eq.(6) gives an equation that relates refractive index and absorption coefficient with the real and imaginary parts of the electrical susceptibility

$$n - j\frac{\alpha}{2k_0} = \sqrt{1 + \chi' + \chi''}. \tag{8}$$

Resonant absorption and refractive index

The motion induced in each bound charge in a dielectric medium by an electric field can be considered as a classical harmonic oscillator system. The relation between polarization density and electric field is described by the second order differential equation

$$\frac{\partial^2 P}{\partial t^2} + \sigma \frac{\partial P}{\partial t} + \omega_0^2 P = \omega_0^2 \epsilon_0 \chi_0 E, \tag{9}$$

where σ, ω_0, and χ_0 are constants. The displacement of each charge x and the applied force F are related by

$$\frac{\partial^2 x}{\partial t^2} + \sigma \frac{\partial x}{\partial t} + \omega_0^2 x = \frac{F}{m}, \tag{10}$$

where m is the mass of the charge and σ is the damping coefficient. $\omega_0 = \sqrt{\frac{\kappa}{m}}$ is the resonance angular frequency and κ is the elastic constant. The force F is equal to eE and the polarization density is $P = Nex$, where e is the electron charge, and N is the number of charges per unit volume. The dielectric medium is completely characterized by its response to monochromatic harmonic fields. $E(t) = Re[Eexp(j\omega t)]$ and $P(t) = Re[Pexp(j\omega t)]$ can be substituted into Eq.(9). Equating the coefficients of $exp(j\omega t)$, we get

$$P = \epsilon_0 [\frac{\chi_0 \omega_0^2}{\omega_0^2 - \omega^2 + j\sigma\omega}] E. \tag{11}$$

P is related to the frequency dependent susceptibility by the relation $P = \epsilon_0 \chi(\upsilon) E$, which gives

$$\chi(\upsilon) = \chi_0 \frac{\upsilon_0^2}{\upsilon_0^2 - \upsilon^2 + j\upsilon\Delta\upsilon}, \tag{12}$$

where $\upsilon_0 = \frac{\omega_0}{2\pi}$ is the resonance frequency, and $\Delta\upsilon = \frac{\sigma}{2\pi}$.

The real and imaginary parts of $\chi(\upsilon)$ are given by

$$\chi'(\upsilon) = \chi_0 \frac{\upsilon_0^2(\upsilon_0^2 - \upsilon^2)}{(\upsilon_0^2 - \upsilon^2)^2 + (\upsilon\Delta\upsilon)^2} \tag{13}$$

$$\chi''(\upsilon) = -\chi_0 \frac{\upsilon_0^2 \upsilon\Delta\upsilon}{(\upsilon_0^2 - \upsilon^2)^2 + (\upsilon\Delta\upsilon)^2} \tag{14}$$

The real and imaginary parts of the refractive index are plotted in Fig. 3.

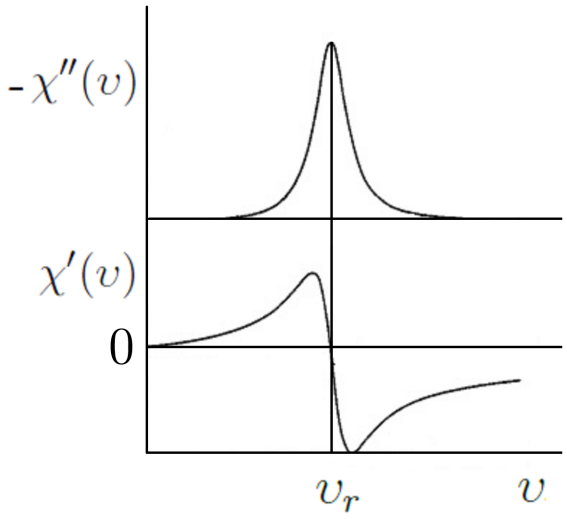

Figure 3: The imaginary and real parts of the susceptibility of a resonant dielectric medium. υ_r is the resonance frequency.

$\chi'(\upsilon)$ is positive below the resonance frequency, zero at resonance, and negative above resonance. $-\chi''(\upsilon)$ has a peak value of $(\upsilon_0/\Delta\upsilon)\chi_0$ at $\upsilon = \upsilon_0$. The real part of the susceptibility contributes at all frequencies near and below the resonance frequencies of a dielectric material, whereas the imaginary part is confined near the resonance frequency. The relation between susceptibility and α and n as shown in Eq.(8) leads to the frequency dependence of the absorption coefficient and the refractive index of a dielectric medium.

2.2 Interferometric refractometers

Refractometers based on interferometry provide higher sensitivity to the refractive index measurements of a test analyte [20,21]. In interferometric techniques, one of the arms of the interferometer is the reference, while the other arm contains the sample whose refractive index needs to be measured. The addition of the sample causes a phase delay in the light traveling through it by changing its optical path length (OPL). The resulting optical path difference is related to the refractive index of the sample and can be measured by monitoring the changes in the interferometric fringe pattern. In the following section, Michelson and Mach-Zehnder interferometers are chosen to demonstrate the general operating principles of interferometric refractometers.

Interferometry

Interferometry is the use of interference effects to build devices for measuring properties of materials. Interferometry can be used to measure, e.g., wavelengths, imperfections on optical components, distances, and refractive indices. [22].

In Michelson and Mach-Zehnder interferometers, a collimated beam of light from a monochromatic source is split into two by a beam splitter. The two beams travel along two arms of the interferometer. They are then brought back together to produce an interference pattern. If the two superposing waves have the same phase, they undergo constructive interference, leading to a wave of higher amplitude, which is seen as a bright line in the interference pattern. Superposing waves that are in opposite phase undergo destructive interference, leading to dark lines.

The phase difference is a factor of the difference in the optical path length that the two beams traverse.

$$\Delta\phi = \frac{2\pi}{\lambda}\Delta x, \tag{15}$$

where Δx is the optical path length difference, and $\frac{2\pi}{\lambda}$ is the wavenumber k for the wavelength λ.
Constructive interference happens when

$$\Delta\phi = \pm 2m\pi, \qquad m = 0, 1, 2, 3, ... \tag{16}$$

Destructive interference happens when

$$\Delta\phi = \pm(2m+1)\pi, \qquad m = 0, 1, 2, 3, ... \tag{17}$$

An analysis of the interference fringes provides information about the amplitude and phase difference of the two waves. This can be used to learn about the properties of a sample placed in one of the interferometer arms.

Types of interferometers

The working principle of the two common amplitude division interferometers - Michelson and Mach-Zehnder are discussed in this section.

The interferometer design shown in Fig 4 is a Michelson interferometer which produces interference fringes with a constant inclination, i.e. fringes that are parallel to each other [22]. Light from a source is split by a beam splitter M. The beams are directed towards two mirrors, M_1 and M_2. The beams converge again at the splitter and are reflected towards a detector where they produce an interference pattern. When M_1 and M_2 are parallel, circular pattern of fringes form at the detector. The mirror M_1 can be moved to adjust the path difference of the two beams to zero. When the path difference is made equal before introducing a test sample, the behavior of the interference fringes can be attributed completely to the properties of the sample.

The design of a Mach-Zehnder interferometer is shown schematically in Fig. 5. It can be used to accurately measure phase changes between two beams split from a single monochromatic source. Beam from a monochromatic source is split into two beams by a beam splitter BS_1. These two beams are then guided along two paths that form the arms of the interferometer. The beams are then reflected by mirrors M_1 and M_2 and combined by BS_2 to produce interference fringes that are observed by a detector. When an analyte, such as a gas, with an unknown refractive index is present along one of the paths, a change in refractive index causes a phase shift of $\Delta\phi = kL_s\Delta n$, where L_s is the length of the sample, and Δn is the change in refractive index.

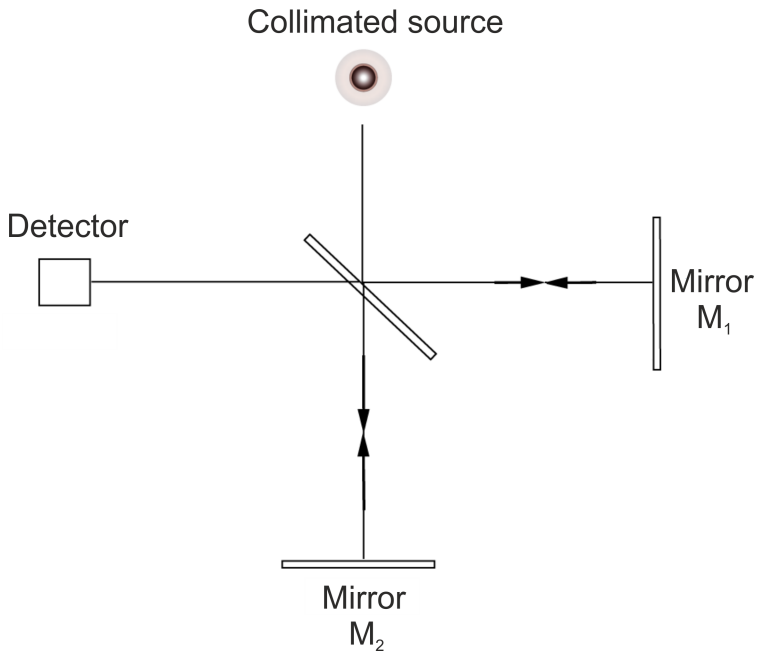

Figure 4: Schematic of a Michelson interferometer.

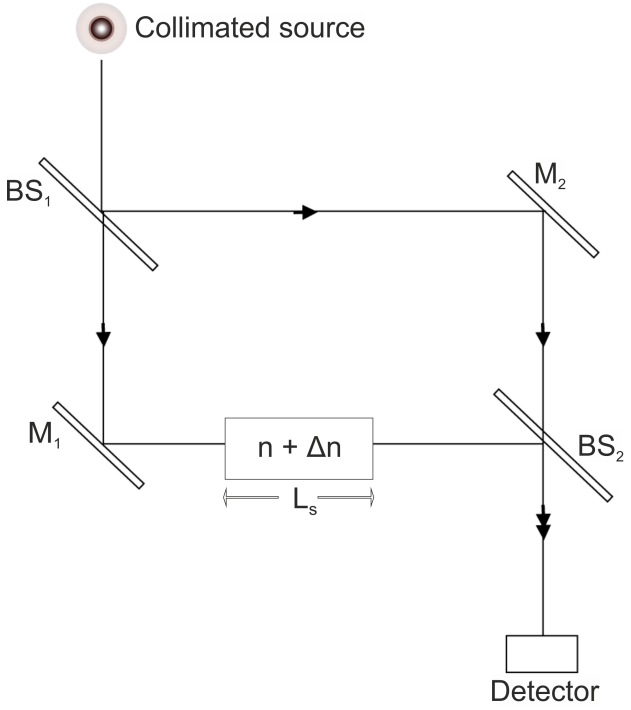

Figure 5: Schematic of a Mach-Zehnder interferometer. Δn is the refractive index of the analyte being measured.

The phase shift is dependent on the refractive index of the gas, and by measuring the phase change at the output, the refractive index of the gas can be calculated. The theory behind these calculations are discussed in section 3.2.

2.3 Optical fibers

Optical fibers are flexible cylindrical waveguides that can guide light mainly along a central core region. They are usually made of silica because of its high mechanical strength and potential for low propagation loss due to absorbance.

The applications of optical fibers includes data transmission, fiber-based lasers, and fiber sensors. They have garnered interest in new sensor technologies because of their compact size and flexible nature. They allow for remote measurements - which is important when sensing hazardous substances [23]. Fiber-based sensors have been used to measure strain, and temperature changes with high resolution [24]. Strain sensors have achieved sensitivities of $2.1 \times 10^6 \epsilon^{-1}$ [25]. This value is called the gauge factor and it is the ratio of the change in electrical resistance of the sensor caused by strain and the electrical resistance of the un-deformed sensor. Sensors based on Rayleigh scattering, Raman scattering, or Brillouin scattering of guided light to provide information regarding the testing environment or sample have also been developed [26, 27].

Optical fiber based refractometers provide accurate measurement of refractive indices of liquids and gases. In this thesis, standard single mode fibers (SMFs) and a HC-PBF were used as two interferometer arms of our refractometer design. This section describes the operating principles of standard optical fibers and photonic crystal fibers. In addition, previous work on optical fiber based refractometers is discussed.

Standard optical fiber

Standard optical fibers have a transparent core region which is surrounded by a transparent cladding. Light is guided along the core of the fiber by total internal reflection (TIR).

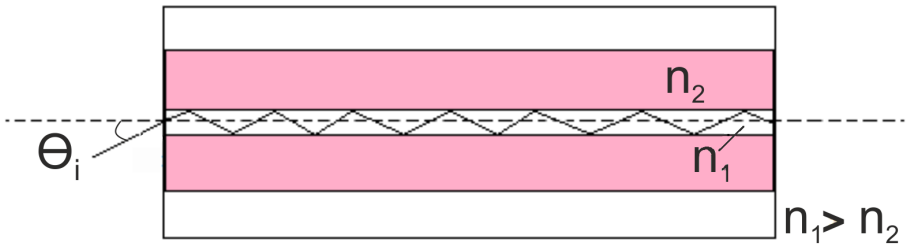

Figure 6: A schematic representation of total internal reflection in a multi-mode fiber. Abbreviations: θ_i is the incident angle, n_1 is the refractive index of the core, and n_2 is the refractive index of the cladding.

The cladding has a refractive index that is lower than that of the core. This causes incident light to bend or refract at the core-cladding interface. The relationship between the angle of refraction and the angle of incidence at the core-cladding interface is given by Snell's law

$$n_1 \sin\theta_i = n_2 \sin\theta_r, \tag{18}$$

where n_1 is refractive index of the core, n_2 is the refractive index of the cladding, θ_i is the angle of incidence, and θ_r is the angle of refraction. Solving for θ_r

$$\theta_r = \sin^{-1}[\frac{n_1}{n_2} \sin\theta_i]. \tag{19}$$

θ_r increases with the increase in θ_i. When θ_r is equal to $\frac{\pi}{2}$, the refracted wave grazes the core-cladding interface.

The angle of incidence for which the angle of refraction is equal to 90°, is called the critical angle

$$n_1 \sin\theta_c = n_2 \sin(90^\circ), \tag{20}$$

$$\sin\theta_c = \frac{n_2}{n_1}. \tag{21}$$

For any angle of incidence greater than the critical angle, the beam will remain confined inside the core. In order to have TIR, the ratio of n_2/n_1 should be less than 1. This means that the refractive index of the incident medium, i.e. the core of the fiber, must be greater than that of the cladding.

When TIR occurs at the core-cladding region of an optical fiber, some of the light intensity is lost to the cladding region as the light travels along the fiber. These are called evanescent waves. To understand how evanescent waves are generated, we need to consider the wave nature of light. When a light wave experiences total internal reflection, a fraction of the energy of the wave penetrates into the cladding region. This happens because some of the wave vector components become complex valued, and the wave experiences exponential decay as it travels in a direction parallel to the direction of the core. A schematic of the evanescent field is shown in Fig. 7.

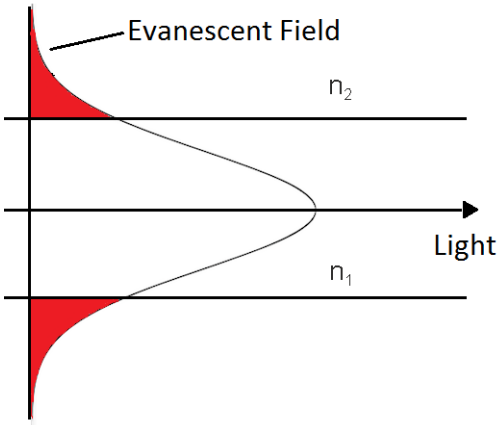

Figure 7: Evanescent field in a single-mode fiber.

The principle of the evanescent field sensor is to make the analyte and evanescent electromagnetic field interact [28–30]. The cladding of an optical fiber can be removed, and the evanescent wave can be made to overlap with a sample by placing the sample in direct contact with the fiber.

Photonic crystal fibers

A new class of optical fibers called photonic crystal fibers (PCFs) have a different guiding mechanism to conventional fibers that make them better suited for gas sensing.

A photonic crystal is a dielectric structure with alternating layers of material with different refractive indices. Optical fibers that incorporated the photonic crystal structure were developed by the research group of St. J. Russell in the 1990s [34–36]. The fibers have an arrangement of small and closely spaced air holes in the cladding along the entire length, and a solid or hollow core. The air holes are fabricated by using a special preform that consists of capillaries of silica glass resembling the form of the final fiber.
Figure 8 shows the schematic of three types of PCFs. The microstructured cladding of such fibers enables light to be guided in two ways; index-guiding and bandgap guiding.

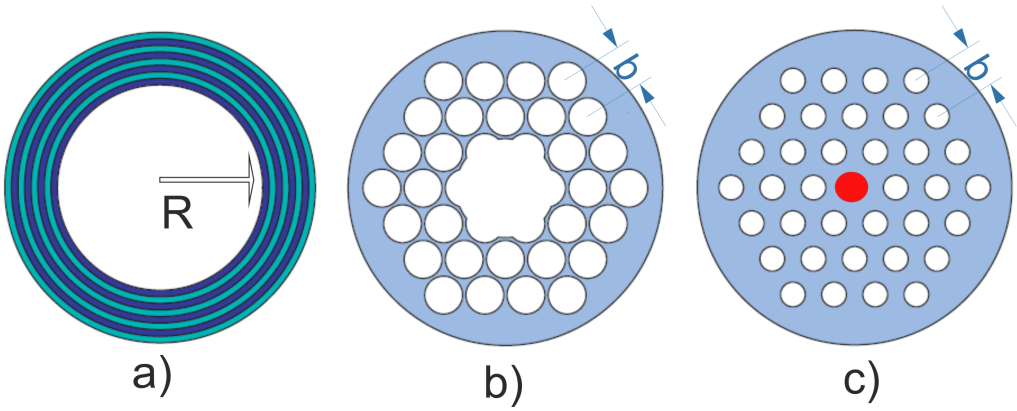

Figure 8: Examples of PCFs. a) Bragg fiber with 1-D periodic cladding. R is the fiber radius. b) 2-D periodic structure with a triangular lattice of airholes and hollow core. b is the spatial period of the holes. c) Holey fiber that confines light in a solid core denoted by red circle. Modeled from [32].

Index-guiding in a PCF can be accomplished in a solid core fiber, as the one shown in Fig. 8(c). Light is guided in a holey fiber by modified-total internal reflection (M-TIR) due to the smaller average refractive index of the cladding relative to the core. The microstructure reduces the effective refractive index of the cladding region. A region of the fiber with a missing air hole has a higher refractive index and becomes the fiber core. Holey fibers have a stronger evanescent field in their cladding region compared to SMFs. Their effective cladding refractive index is wavelength dependent, and at longer wavelengths, the evanescent field extends further into the holes. The airholes in the cladding can work as channels through which an analyte gas or liquid can be introduced into the fiber. Sensors based on such fibers offer higher sensitivity than SMFs [31].

However, index-guided PCFs are still limited in their capacity to overlap light with a sample analyte as a majority of the light is guided through the solid core region with limited interaction with the sample.

Bandgap-guiding fibers

In contrast to index-guiding fibers, a photonic bandgap fiber can confine light in a region of lower refractive index than the surrounding cladding. A photonic bandgap occurs when only a specific set of frequencies of light are allowed to propagate along a waveguide. The first realization of a bandgap-guiding fiber was the Bragg fiber, shown in Fig 8(a). It is based on a 1-D concentric circles of a multilayer material with different refractive indices. The idea of confining light in a region of lower refractive index means that light can essentially be guided within a hollow core. This led to the development of the HC-PBF, which is shown in Fig 8(b). Figure 9 shows an SEM image of the fiber.

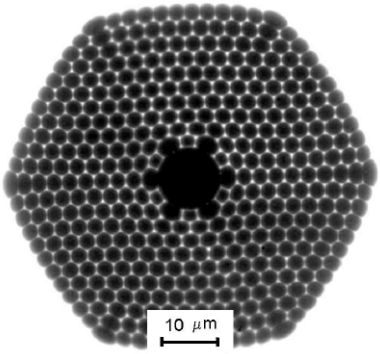

Figure 9: SEM-image of a fiber in which light is guided by the photonic bandgap effect [13].

The concept of trapping light along the core of a fiber using the bandgap effect was first predicted in 1991 by Philip Russell [34]. It was later demonstrated by Birks *et al.* [35]. Optical properties of photonic crystals along one dimension can be altered by breaking the periodicity of the crystal structure [36]. A forbidden gap is created in all but one direction along the fiber, along which light can be guided. Similar to electrons that lie in the electronic bandgap, a bandgap guiding fiber prohibits the guidance of frequencies of light that lie in the photonic bandgap.

The microstructured cladding of the fiber induces incident light to reflect and refract at the glass-air interfaces. This will cancel out a band of wavelengths in those directions along the fiber [33]. This phenomenon is described using a 1-D photonic crystal structure in Fig. 10.

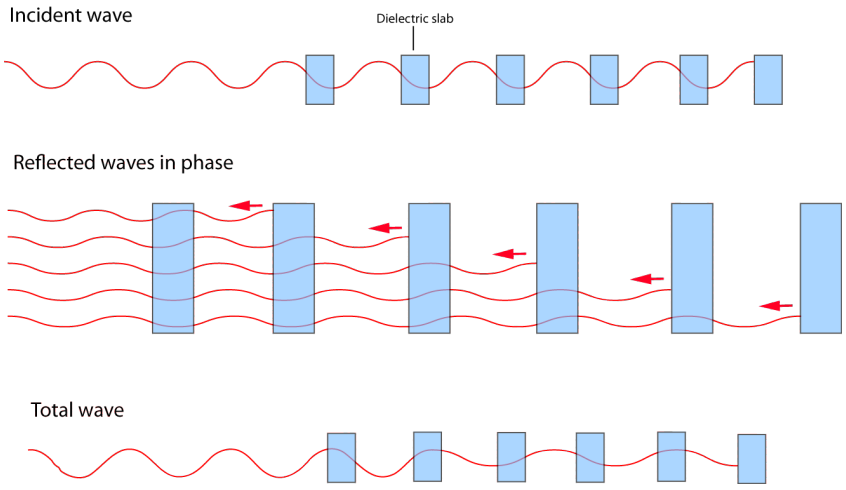

Figure 10: 1D bandgap effect on incident light. Light is partially reflected off each dielectric layer. Modeled from [33].

In a HC-PBF, the 2-D photonic bandgap created by the microstructured cladding

channels light into the hollow core along the longitudinal direction of the fiber. The hollow core can act as a sample cell for light and test analytes. This allows the best possible overlap for sensing applications.

The HC-PBF used in this thesis was a HC-1550-02 (NKT Photonics) fiber. It is designed to operate at a wavelength range of 1490 nm - 1680 nm. The core diameter is 10 μm and has a mode field diameter of 9 μm. The fiber can be filled with a gas analyte in a short time because of the relatively large core size and the microstructured cladding. The gas filled air holes increase the overlap between analyte and the mode field propagating through the fiber. HC-PBFs are also insensitive to bending. The effect of the fiber material on the guided light in the hollow core is significantly low [37]. In a typical HC-PBF, the fractional power in silica material is only 1.5 - 2% [38], and the rest remains confined to the hollow core. This is important in fiber-based sensors as the influence of fiber properties on measurements reduces sensor sensitivity. Lower absorption at the silicon cladding also leads to lower losses [39]. One issue with bandgap-guiding fibers such as the HC-PBF is that they operate at a limited wavelength range.

Fiber-based refractometers

Initial studies on fiber-based refractometers involved SMFs submerged in a liquid analyte whose refractive index was to be measured. Fresnel reflection of light at the fiber-liquid interface at the fiber end was used to calculate the refractive index of the liquid [40]. Fiber based refractometers employing D-shaped single-mode fibers that utilize total internal reflection heterodyne interferometry to calculate the refractive index of liquids have been proposed that provide a resolution of 3×10^{-5} RIU [11]. Light from a reference medium with a higher refractive index is incident on a test medium with a lower refractive index. If the beam undergoes total internal reflection, phase shifts in the P- and S- polarizations are induced in the output beam. Using the calculated phase shift, along with the known refractive index of the first medium, and the angle of incidence, the refractive index of the second medium can be calculated.

PCFs with the air-hole structure provide better overlap between light and analyte than conventional all-solid optical fibers. The potential of photowriting Bragg gratings into the solid core of a index-guiding PCF to measure the refractive index of liquids was investigated by C. Minh *et al.* in 2006 [41]. They employed two fiber designs to measure liquids whose refractive index where between 1.29 and 1.45. One of the fiber exhibits a six hole cladding, and the other a two ring triangular structure. The liquids are inserted in the holes of the PCFs which creates a shift in the resonance frequency of the FBGs in the core. The PCF design allows a good overlap between the liquids and the propagating light in the core, and measurement resolution of the order of 10^{-4} was observed from both designs. When the refractive index of the liquid approached the effective refractive index of the guiding mode of the fiber, resolution of 2×10^{-5} and 7×10^{-6} were observed for the two-ring and six-hole designs, respectively.

Evanescent wave gas sensing can be achieved in a index-guided PCF with the study of the absorption peaks of acetylene using a 75 cm long fiber [42]. Pure acetylene gas was diffused into the air-holes of the PCF by maintaining the gas pressure inside the chamber at 103 kPa higher than the ambient pressure. Light from a wavelength tunable laser was scanned over 1520 to 1542 nm at 1 pm steps. The gas was made to interact with the evanescent field of the guided light in the core. Output end of the PCF was directly coupled to a power meter to measure the change in power due to analyte absorption. The absorption spectrum of acetylene achieved by Y. L. Hoo *et al.* over the measurement wavelengths is shown in Fig. 11.

The gas sensing capabilities of a HC-PBF was demonstrated by Ritari *et al.* [13]. The gas was diffused directly into the hollow core of the fiber, which achieved the best possible overlap with light. For the measurement of the absorption spectrum of acetylene gas, a 1-m long HC-PBF was filled with acetylene and a tunable laser with a wavelength step of 1 pm was scanned over the P-branch of the $\upsilon_1 + \upsilon_3$ band. They represent the set of wavelengths where rotational-vibrational transitions give rise to pronounced resonances [43]. Figure 12 presents the results of the measurement.

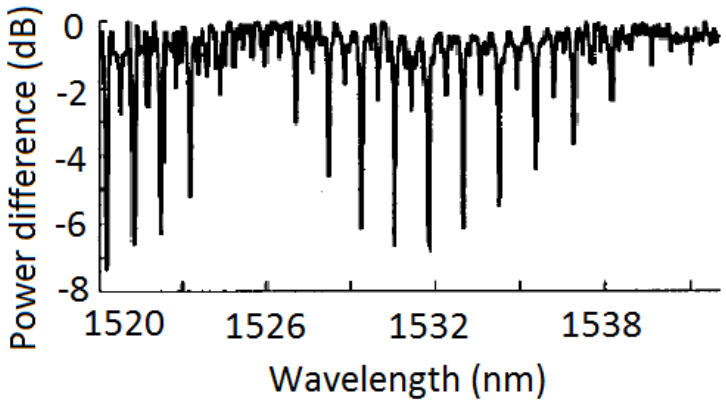

Figure 11: Absorption spectrum of near 100% acetylene with 75 cm long PCF [42].

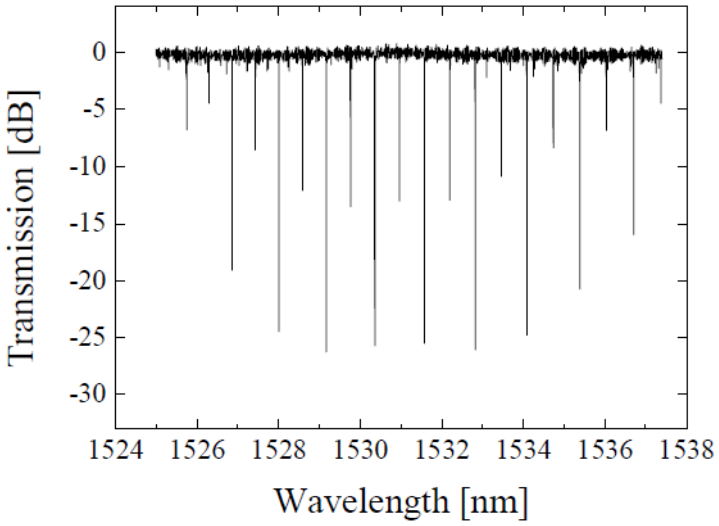

Figure 12: Normalized absorption spectrum of the P-branch of the $\upsilon_1 + \upsilon_3$ band of acetylene at 10 mbar in 1 m long HC-PBF measured using a tunable laser (step size 1 pm) [13].

The absorption spectrum of volatile gases such as hydrogen cyanide, methane, etc. was also measured using this setup.

2.4 Sensor performance parameters

The performance of a sensor depends on a number of parameters such as sensitivity, resolution, and accuracy. It is important to understand these parameters to reliably interpret sensor measurements.
Sensitivity is defined as the change in the output of the sensor per unit change in the parameter of the analyte that is being measured. The sensitivity of the refractometer used in this study is dependent on the relation between the change in phase and amplitude of the interference fringes at the output with the change in refractive index of the analyte. The sensitivity of the device for the real refractive index change can be expressed as

$$S = \frac{\Delta\phi}{\Delta R}, \tag{22}$$

where $\Delta\phi$ is the change in phase which is seen as the movement of interference fringes, and ΔR is the change in refractive index. The degree of overlap between light and the analyte is directly proportional to the device's sensitivity. In addition, it is also conditional to the specifications of the CCD camera employed for detection, such as the signal-to-noise ratio. This relates to the capacity of the measurement signal to stand out from the surrounding noise.

Resolution is the smallest measurement a sensor can detect. For example, the human eye can detect an object that is approximately 0.1 mm in size. The resolution of a refractometer sensor depicts the smallest change in refractive index of an analyte that the device can observe. The resolution of the device presented here is determined by the number of pixels in the CCD camera and their size in relation to the projected image. The projected image should be larger than the pixel size for the camera to accurately reproduce the image. If the smallest image that the camera can detect is a, then the resolution of the refractometer can be calculated from its sensitivity

$$R = \frac{a}{S}. \tag{23}$$

Accuracy is defined as the maximum difference between the actual value and the indicated value at the output of a sensor. Precision gives an account of the reproducibility of a measurement. A high precision sensor will produce the exact output over repeated measurements of an analyte.

3 Experimental setup

In this chapter, an experimental realization of a gas refractometer based on using a HC-PBF in a Mach-Zehnder type interferometer is presented. We carry out performance measurements over the wavelength range of 1525 nm - 1545 nm where the P-branch of the $\upsilon_1 + \upsilon_3$ vibration band gives rise to a number of pronounced resonances in acetylene [13]. The aim is to calculate the complex refractive index of pure acetylene.

3.1 Gas refractometer

The refractometer was designed by Igor Shavrin *et al.* with a HC-PBF as a sample cell and waveguide in a Mach-Zehnder-type interferometer [12]. A schematic is depicted in Fig. 13.

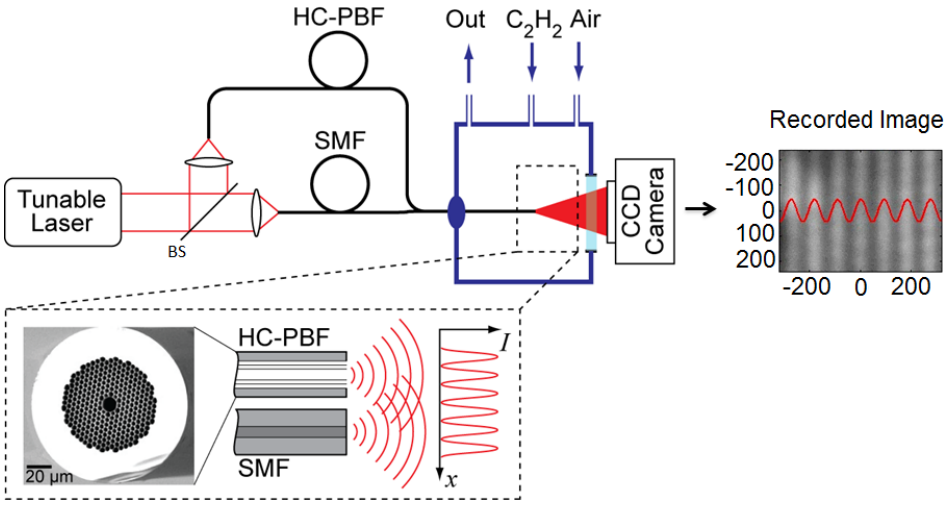

Figure 13: Gas refractometer setup [12].

Light from a wavelength tunable laser (GN Nettest TUNICS-Plus), operating in the near infrared region, was split using a 50/50 beam splitter (BS) cube and focused into the two arms of the interferometer. A SMF and a HC-PBF (NKT Photonics, HC-1550-02) were used in the reference and sample arms, with lengths 19.5 cm and 27.9 cm, respectively. These lengths were chosen to ensure nearly equal optical path lengths of the arms. A scanning electron microscope (SEM) image of the HC-PBF, and an illustration of the interaction between light from the two fibers inside the chamber is shown in the inset of Fig. 13.
The two fibers are glued along their sides inside the chamber so that the outgoing light forms an interference pattern. The chamber has a glass window that allows a CCD camera to capture the fringes. The ends of the fibers are placed in a sealed chamber to facilitate the filling of the HC-PBF with acetylene at a defined pressure. The other end of the HC-PBF is open to ambient air, which causes the gas to flow along the fiber at a constant rate.

Change in optical path length of the HC-PBF with the addition of acetylene-air mixture into the HC-PBF was seen as fringe movement by the camera. Absorption of light by acetylene was seen as a change in amplitude of the fringes. The fringes were recorded as images by a CCD camera with a 640 by 480 pixels resolution. The images were analyzed using matlab code that applied 2-D Fourier transformation to identify the average fringe amplitude and phase for each image.

A second vacuum chamber was added to seal the open end of the HC-PBF as shown in Fig. 14.

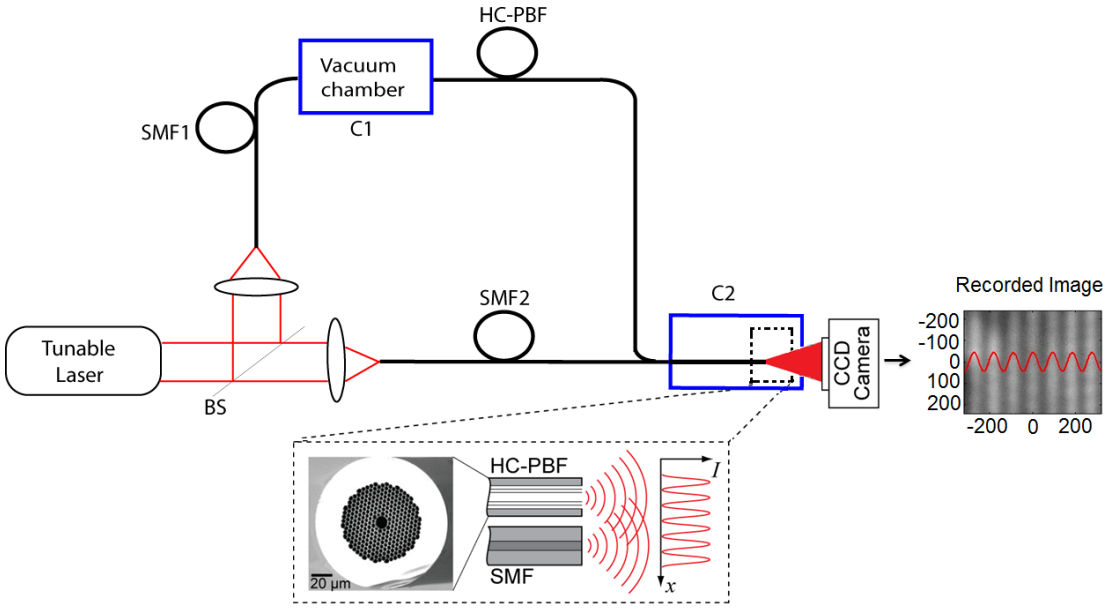

Figure 14: Modified gas refractometer setup.

Light after the BS was guided into the HC-PBF inside the chamber C_1 using a second SMF (SMF1). 12 kPa of acetylene gas was let into the chamber C_2 and allowed to diffuse into the HC-PBF for 10 minutes. Both ends of the fiber were maintained at chamber pressure, and the gas distributed uniformly along the length of the HC-PBF.

The OPL of the sample arm of the refractometer increases because of the addition of the SMF1. In order to compensate for the increase in OPL of the sample arm, the OPL of the reference arm was increased by adding two mirrors. The distance between the two mirrors was modified to minimize the fringe movement to 2π per 10 nm change in wavelength. This denotes a near equal OPL along both arms. The design is shown in Fig. 15.

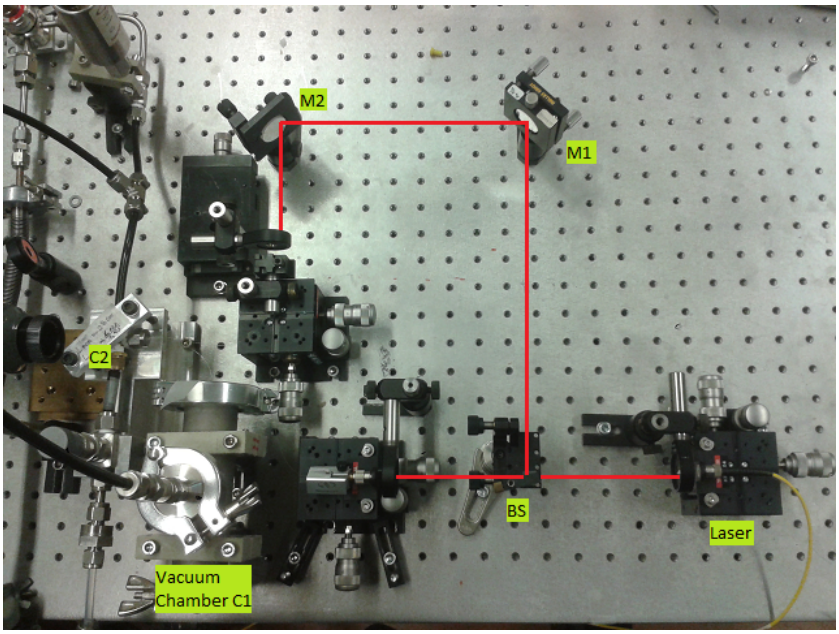

Figure 15: Photograph of the experimental setup with two vacuum chambers. M_1 and M_2 are two mirrors that were used to increase the OPL of the reference arm. OPL is marked as a red line.

3.1.1 Vacuum chamber design

We used a "T" shaped stainless steel chamber to enclose the open end of the HC-PBF. The horizontal pipes were 75 mm wide and 140 mm in length. The vertical pipe was 30 mm wide. The smaller pipe was fitted with a Swagelok adapter and the chamber was connected to chamber C_2 using a 6 mm plastic tube. Stainless steel was preferred as the chamber material because it is non-reactive to acetylene.

To guide light from the SMF1 to the HC-PBF inside the vacuum chamber C_1, both fibers were placed on a V-groove. Figure 16 illustrates the arrangement inside the chamber. In order to achieve a clear detection of the interference fringes by the camera, the coupling loss should be low. Two 3-D translators were used to align SMF1 and the HC-PBF placed in the V-groove. A screw was drilled through one end cap of $C1$ and the V-groove, and bolted to hold them in place. This made it easier to seal the V-groove-fiber system inside the chamber once they were glued in position. Distance between the two fiber ends were adjusted and the percentage of coupled light was measured using a power meter.

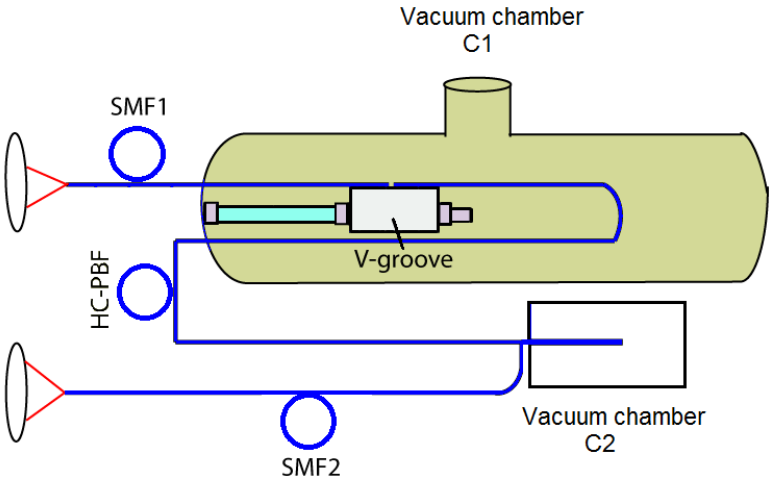

Figure 16: Scheme of the design used to guide light into the HC-PBF.

When maximum coupling between the two fibers was achieved, they were glued firmly in place. Two additional holes were drilled through the end cap of C_1 - one for HC-PBF and second for the free end of SMF1, and then sealed with glue. O-rings were used to ensure a vacuum seal when the V-groove system was enclosed inside the chamber. The endcaps were fixed securely using clamps. A photograph of the final design is presented in Fig. 17. SMF1 is shown with one end of the fiber inside C_1 where light is guided into the HC-PBF. The other end of the HC-PBF comes out of the end cap and is placed inside C_2 along with the SMF2 from the reference arm. This can be seen in Fig. 18. The photograph of C_2 was taken at the conclusion of the experiments.

Measurements of the coupling efficiency between SMF1 and HC-PBF were repeated after sealing C_1 to make sure that the fibers were still held in place in the V-groove.

The valve tap was used to flush the refractometer after a measurement. The fibers were glued parallel to each other inside C_2. The intereference fringes were observed by an infrared viewer through a glass window in the chamber, and the image from the eye piece was focused onto the CCD camera.

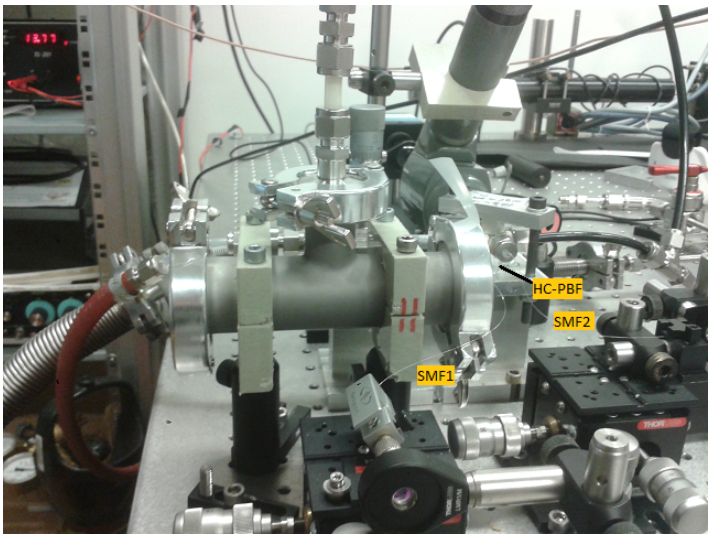

Figure 17: Photograph of the vacuum chamber C_1. SMF1 enters C_1 via a hole drilled in the end cap. The other end of the HC-PBF is taken out through a second hole and placed inside the second chamber.

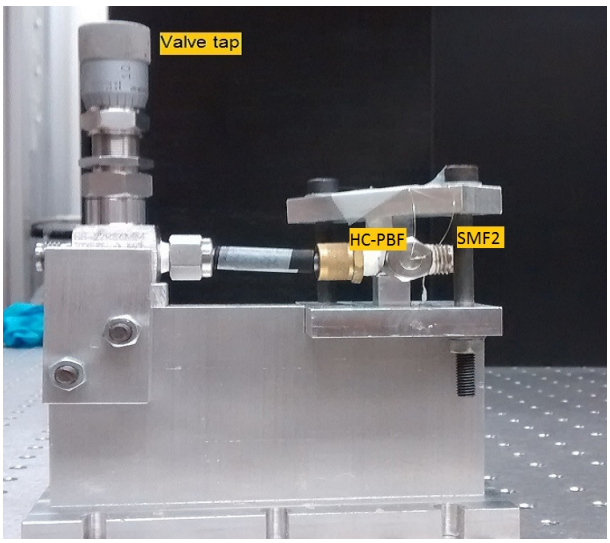

Figure 18: Photograph of the vacuum chamber C_2. HC-PBF and SMF2 are glued parallel to each other inside the chamber.

3.2 Refractometer model

A fiber based Mach-Zehnder interferometer similar to the design illustrated in Fig 19 was implemented to build the refractometer in our experiment. An SMF was used in the reference arm and a HC-PBF was used in the sample arm. The HC-PBF worked as a waveguide and an analyte containing cell. Light from a monochromatic source is guided into the refractometer. The beams of light from the two arms are made to overlap at the output end to from interference patterns. The change in effective refractive index of the fiber because of the gas causes a change in the optical path length of the sample arm [44].

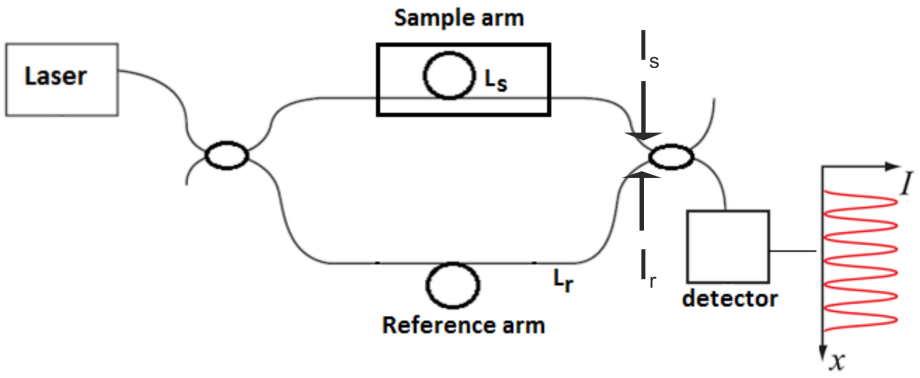

Figure 19: Mach-Zehnder interferometer with a HC-PBF as the sample arm. I_s and I_r are the intensities along the sample and reference arms respectively. The intensity distribution of the interference pattern along x-axis is observed by the detector.

Assuming that the refractive index of the sample arm is a function of its effective index and the refractive index of the sample,

$$n_s = n_{eff} + \delta n_{gas}. \tag{24}$$

Optical path difference in the interferometer is dependent on n_s, and is related to phase change $\Delta\phi$

$$\Delta OPD = \Delta n_{HCF} L_s = \Delta\phi \frac{\lambda}{2\pi}, \tag{25}$$

where $\Delta\phi$ is the phase change in response to ΔOPD.

The refractive index dependence on path length means that the change in effective index of the sample fiber induced by the gas makes the OPLs of the two arms unequal. This causes a phase difference between the two beams of the interferometer, which is observed as a change in the position of the interference fringes at the output. In addition to the change in effective refractive index of the fiber, the gas also absorbs light, which translates to a change in fringe amplitude. By analyzing the change in position, and amplitude of the interference fringes over a range of wavelengths, the

complex refractive index of the gas can be found.

Intensity at the output end of the refractometer is given by

$$I = I_s + I_r + 2\sqrt{I_s I_r}\cos\phi, \tag{26}$$

where I_s is the intensity in the sample arm, I_r is the intensity in the reference arm, and ϕ the phase difference between the two arms. Considering light entered the two arms at equal phase, the phase difference at the output depends on the acquired phase by optical waves propagating in each arm and the light wavelength.
For a fiber with an effective refractive index $n_i(\lambda)$ of a guided mode, the acquired phase is

$$\phi_i(\lambda) = \frac{2\pi n_i(\lambda) L_i}{\lambda}, \qquad i = r, s. \tag{27}$$

The expression for the phase difference as the beams travel through the two arms of the interferometer is given by

$$\phi(\lambda) = \frac{2\pi}{\lambda}[L_s n_s(\lambda) - L_r n_r(\lambda)], \tag{28}$$

The introduction of the analyte into the sample fiber causes a change in the effective refractive index of the fiber. Consider that this change in effective index is seen as a small perturbation

$$n_s(\lambda) = n_{s0}(\lambda) + \delta n_a. \tag{29}$$

Substituting (29) into (28) we get,

$$\phi(\lambda) = \frac{2\pi\delta n_a L_s}{\lambda} + \frac{2\pi}{\lambda}[n_{s0}(\lambda)L_s - n_r(\lambda)L_r] = \frac{2\pi\delta n_a L_s}{\lambda} + R(\lambda). \tag{30}$$

The first term describes the contribution of the analyte's refractive index to the phase difference, and $R(\lambda)$ is the intrinsic response of the interferometer in the absence of the analyte. Difference in properties of the two fibers, such as dispersion, contribute to $R(\lambda)$. Even with the optical lengths of the two fiber arms of the interferometer are made equal, they are only equal for a particular wavelength of light. The presence of the HC-PBF makes the accurate measurement of $R(\lambda)$ difficult. Instead, we carry out two refractive index measurements, one for a known gas, and another for the analyte, and cancel out the contribution of fiber dispersion.

The phase difference of the two measurements carried out on a gas of known refractive index and analyte is

$$\phi_1 - \phi_2 = \frac{2\pi L_s}{\lambda}[\delta n_{a1} - \delta n_{a2}]. \tag{31}$$

The expression for the absolute refractive index of a sample is given by

$$n_\lambda = n_\lambda^{air} + \Delta\phi\frac{\lambda}{2\pi L_s}, \tag{32}$$

where n_{λ}^{air} is the refractive index of air used as a reference, $\Delta\phi$ is the phase difference between reference and sample gas measurements.

Amplitude of the interference fringes is dependent on the absorption coefficient of an analyte in the sample fiber. The intensity of the interference pattern is maximal for constructive interference and minimal for destructive interference. They are given by

$$I_{max} = I_s + I_r + 2\sqrt{I_s I_r}, \phi = 0. \tag{33}$$

$$I_{min} = I_s + I_r - 2\sqrt{I_s I_r}, \phi = \pi. \tag{34}$$

Fringe amplitude is given as

$$A(\lambda) = 2\sqrt{I_s I_r(\lambda)}. \tag{35}$$

The intensity in the sample arm is dependent on the wavelength because absorption by the sample analyte is wavelength dependent. Intensity in the sample arm is given by

$$I_s(\lambda) = \frac{A^2(\lambda)}{4I_r} \tag{36}$$

By measuring the fringe amplitude at the output of the refractometer, the transmission spectrum and absorption coefficient can be calculated by

$$T(\lambda) = \frac{I_1}{I_2} = \frac{A_1^2}{A_2^2}, \tag{37}$$

$$\alpha(\lambda) = \frac{\log(T(\lambda))}{L_s}, \tag{38}$$

where I_1 and I_2 are the intensities and A_1 and A_2 are the amplitude measurements of the reference gas and sample gas respectively.

Fringe shift measurement provides information about the relative change in refractive index in the interferometer. In order to obtain the absolute refractive index, a reference point is needed from which the number of fringes moved can be counted. This point can be the zeroth order fringe. However, to determine the zero order fringe requires the path lengths of the reference and sample arms of the interferometer to be precisely equal. In addition, identifying the zeroth fringe is difficult with a monochromatic light source.
We adopt a different approach that involves using the refractive index of a known gas as reference in order to calculate the absolute refractive index of the sample.

The refractive index of air at various pressures can be calculated using Edlen's equation to a precision of 10^{-7} RIU [46, 47].

3.3 Laser

A wavelength tunable laser source was required for this thesis to calculate the wavelength dependence of the complex refractive index. We used a GN Nettest TUNICS-plus external cavity fiber laser with a wavelength range of 1470 - 1570 nm. It has an adjustable scan speed of 1 to 100 nm per second, and a wavelength setting resolution of 1 pm. The output fiber is a single mode fiber (SMF-28) which has a low loss of around 0.20 dB/km at wavelengths relevant to this study.

It is based on a modified Littman-Metcalf configuration, with a laser diode as the light source. It has a very short cavity which maximizes mode spacing. This guarantees a single-mode operation. A diffraction grating is used to tune the wavelength. A mirror reflects the first-order beam back to the laser diode. This allows for stronger wavelength sensitivity as the wavelength dependent diffraction occurs twice instead of once per resonator round trip. The novel optical design ensures smooth scans, high output power, and good long-term stability [48].

3.4 Pressure gauges

The pressure inside the two chambers was measured using two absolute pressure transducers (1 MKS Baratron Type 722A and 1 Omega PX603) that convert pressure into a linear DC voltage output. They consist of a sensor and a signal conditioner. The sensor includes a variable capacitor and a pressure inlet tube connected to chamber inside the sensor body. One of the walls of the chamber is a metal diaphragm. The front side of the diaphragm is open to the gas whose pressure is being measured. The opposite side is the reference side of the diaphragm, which faces a firmly mounted ceramic disc with two electrodes. The inlet port is at the opposite side of the diaphragm. The reference side of the diaphragm is maintained at a pressure below the resolution of the instrument.

The pressure of the gas under measurement deflects the diaphragm towards the two electrodes. The change in distance to the diaphragm causes an imbalance in the capacitance of the electrodes. A frequency oscillator converts this imbalance into DC voltage. The output signal is scaled to the range of the transducer. A computer is used as a display unit for the pressure readout.

3.5 Camera

The interference fringes at the output end of the refractometer were first converted into a visible image using a mounted infrared scope. The image was then focused onto the CCD of a monochromatic camera (Imaging Source DMK 21BU04) using a focusing lens with a focal length of 10 mm. The camera has a sensitive 1/4" CCD sensor (Sony ICX098BL) that captures up to 60 images per second. It has a resolution of 640 by 480 pixels, and the size of each pixel is 5.6 μm by 5.6 μm.

At each measurement step, the camera records one image. Figure 20 presents

an image of the interference fringes recorded by the camera. The sequence of images recorded for all steps during measurement are Fourier transformed to find the spatial frequency of the interference pattern, while other frequency components are considered as noise. The Fourier transformed image is depicted in Fig. 21.

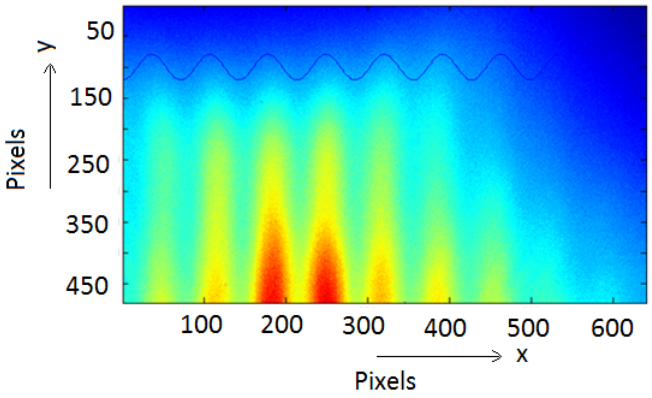

Figure 20: Recorded image of interference fringes. Red color denotes areas of higher intensity and blue denotes areas of lower intensity in the fringe image captured by the camera.

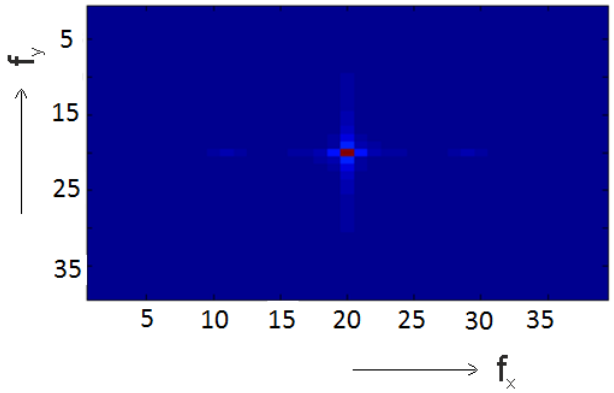

Figure 21: Fourier transformed spatial frequency. Two bright spots appear on either side of zero order and correspond to fringe spatial frequency.

The dependence of fringe position on refractive index can be extracted from the image sequence. It is important that the fringe shift is not larger than $\pm\pi$ to avoid phase ambiguity. This is resolved by ensuring that the optical path difference change is less than half of the wavelength between two images. In order to achieve this, the

recording frame rate of the CCD camera is kept sufficiently high, and wavelength steps are made small.

For simplicity, the intereference fringes at the output end of the interferometer is represented as sinusoidal waves, as shown in Fig. 22.

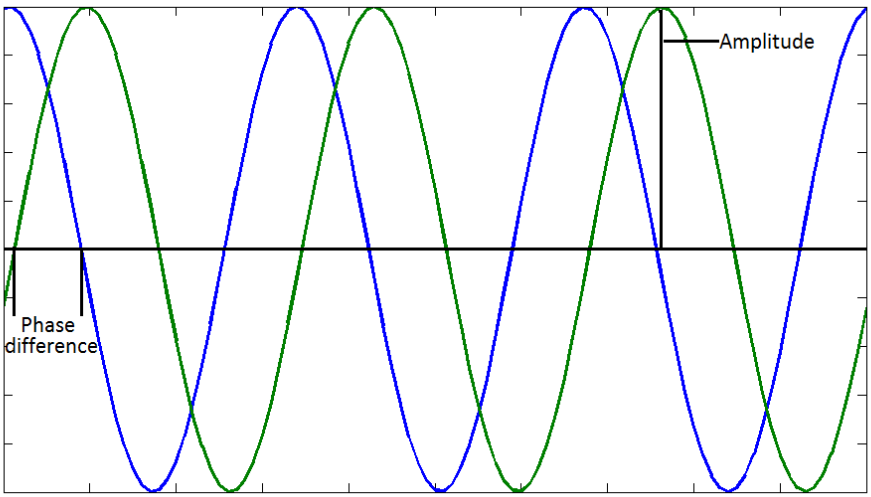

Figure 22: Two light waves out of phase depicted as sine waves.

The amplitude and phase of the fringes is a function of the absorption coefficient and the refractive index of the analyte, respectively.

3.6 Measuring process

The different stages of the measurement procedure is shown in Fig. 23. Each step is explained in detail below.

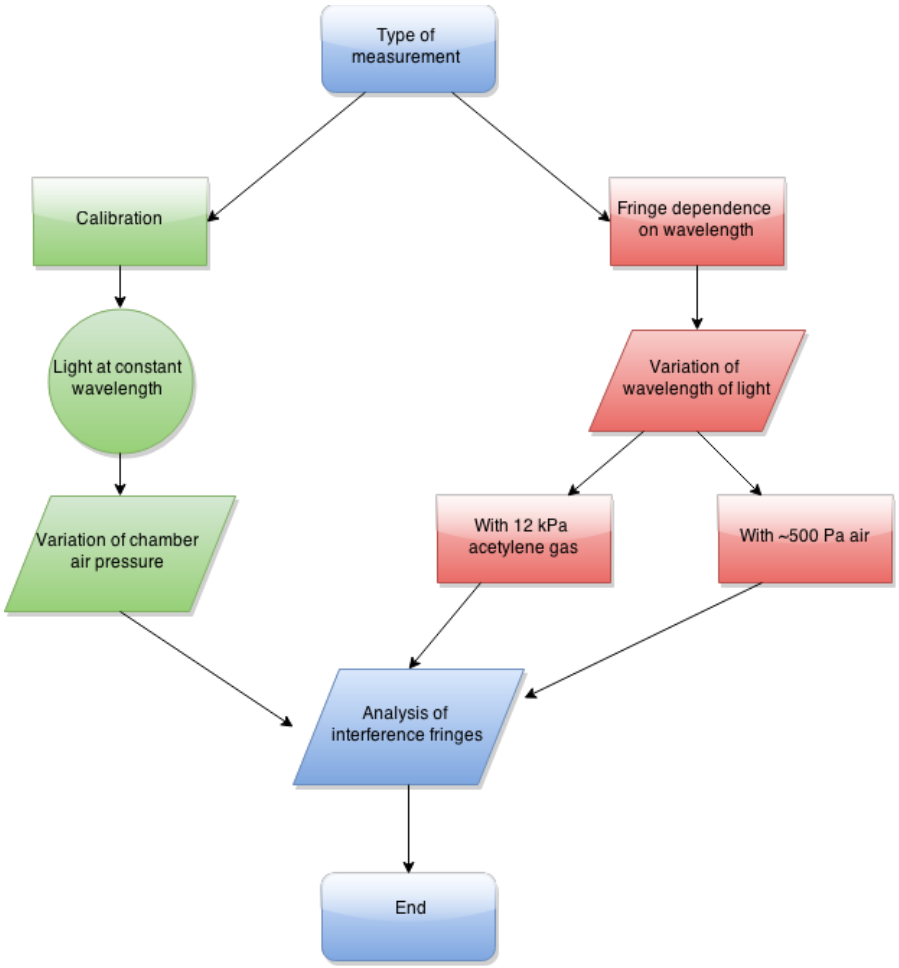

Figure 23: Flow chart of the measurement procedure.

Calibration measurement

The laser was kept at a constant wavelength of 1525 nm and a power of 8 mW, while the pressure inside the chamber C_2 was varied using an inlet and an outlet valve. Using the input from the pressure gauge as reference, pressure inside the chamber was increased from atmospheric pressure to 130 kPa in steps of 5 kPa by letting compressed air into the chamber through the inlet valve. At each step, the pressure inside the chamber was allowed to normalize for about a minute for averaging. The steps were repeated in reverse order by bringing the pressure inside C_2 back to 1 atmosphere by letting air out through the outlet valve.

Fringe dependence on wavelength with acetylene

The two chambers shown in Fig. 14 were evacuated to a pressure of 500 Pa using a roughing vacuum pump. These pumps are used to create a rough vacuum close to 0.1 Pa from atmospheric pressure. Achieving a lower pressure than 500 Pa was not possible due to leaks in the tubing used in the system. The analyte was let into the refractometer through C_2 using an inlet valve. Before the start of the measuring process, the gas was allowed to diffuse uniformly along the length of the fiber, which was found to take about 10 minutes. The wavelength of the tunable laser source was scanned over the selected wavelength steps of 5 pm and 1 pm. The interference fringes at each step was recorded as an image by the camera.

Fringe dependence on wavelength with air

The wavelength dependence of fringe amplitude and phase with 500 Pa air was measured over the same wavelength range steps as for the analyte. This was performed to obtain information about the inherent refractometer properties. The measurement is used as a reference for the final analyte refractive index calculation.

Acetylene was evacuated from the refractometer system using the vacuum pump and the pressure inside the refractometer was allowed to stabilize before starting the measurement. The valve leading to the vacuum pump was closed after reaching the desired pressure in order to avoid oil from the pump leaking into the refractometer.

4 Measurement results

Initial measurements were carried out on the refractometer design developed by Igor Shavrin, *et al.* [12], which is schematically depicted in Fig. 13. The refractometer design presented in the paper achieved spectrally resolved measurements of both real and imaginary parts of the complex refractive index of air-acetylene mixture. Their measurement results are presented in Fig. 24. The corrected imaginary and real-valued refractive index of air-acetylene mixture was extracted by subtracting the intrinsic fiber response, and is depicted in Fig. 25. A refractive index resolution of about 4×10^{-7} was achieved [12].

Our measurements using the same refractometer design corroborated the amplitude and phase change results over the same wavelength range. The complex refractive index results obtained by Igor Shavrin *et al.* were employed as the baseline to compare the resolution of the new refractometer design depicted in Fig. 14.

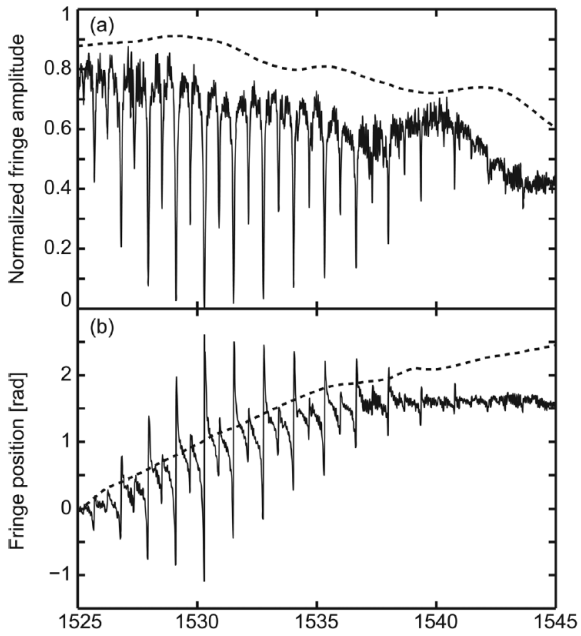

Figure 24: (a) Normalized fringe amplitude and (b) fringe position as a function of the wavelength for air-acetylene gas mixture (solid line) and pure air (dashed line) [12].

The scheme of the modified gas refractometer described in Chapter 3 was used to measure the complex refractive index of 96% pure acetylene gas. Each measurement step is recorded as an image by the CCD camera at the output end of the refractometer.

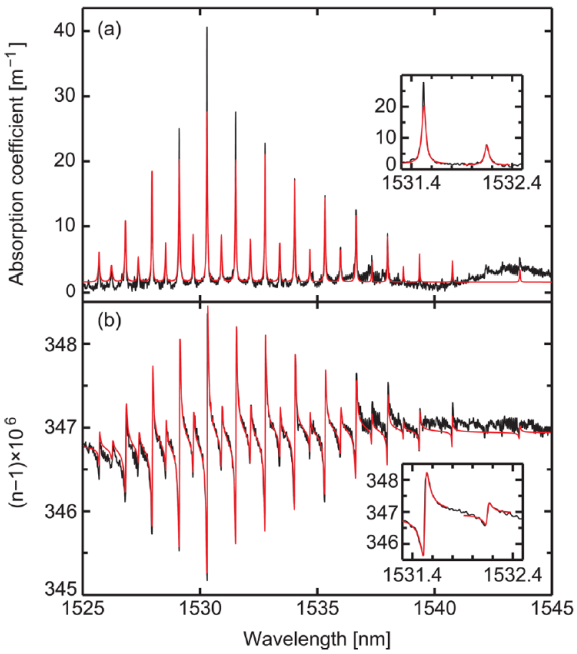

Figure 25: Determined (a) absorption coefficient and (b) refractive index for the air-acetylene mixture (unsmoothed, black). Results obtained by fitting each resonance independently is represented as smooth red curves. Two resonances are shown as examples in the insets [12].

4.1 Calibration measurement

The calibration measurements were carried out to establish a relationship between the change in fringe position and in the real valued refractive index. Changes in the air pressure introduced in the refractometer system led to a variation in the phase. The behavior of the fringe amplitude and phase with changes in the chamber pressure is shown in Fig. 26.

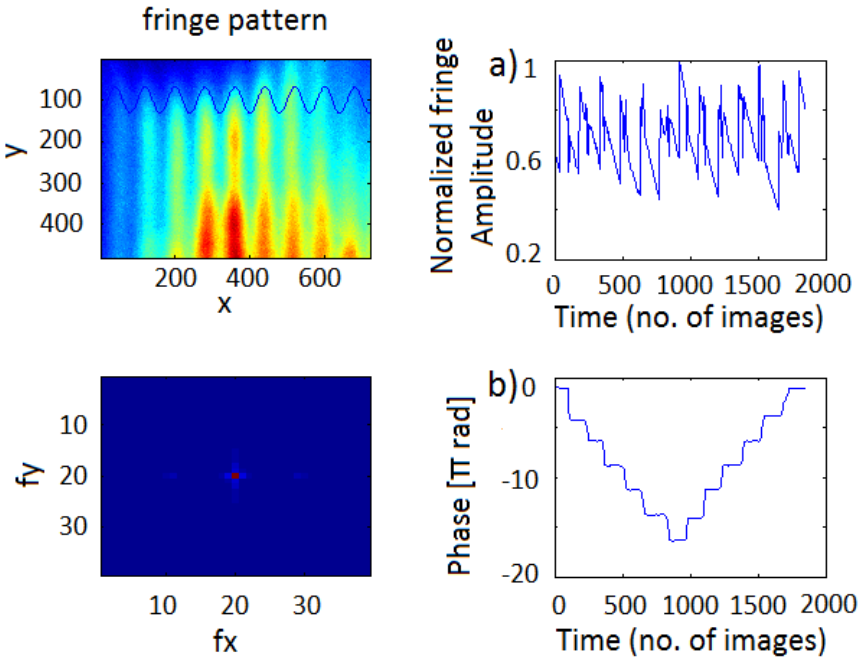

Figure 26: Behavior of (a) fringe amplitude and (b) phase with changes in pressure. The x axis denotes the number of images captured by the camera. The images were analyzed in the order that they were captured, so they describe the passage of time.

Data points across the flat regions in Fig. 26 (b) are time averaged. Refractive index inside the sample arm of the refractometer was calculated using pressure and phase change measurements.
The refractive index calculated using fringe shift was compared to the theoretical results calculated using Edlen's equations for the different air pressures. The dependence of the refractive index of air with fringe shift is shown in Fig. 27.

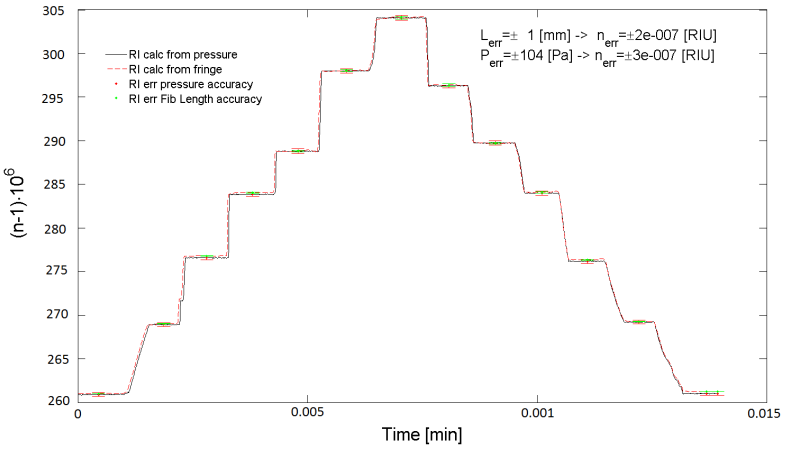

Figure 27: Comparison of calculated refractive index with phase change. L_{err} and P_{err} are the error margins for the length measurement of the HC-PBF and the pressure inside the refractometer. n_{err} is the corresponding error margin in the measured refractive index of air.

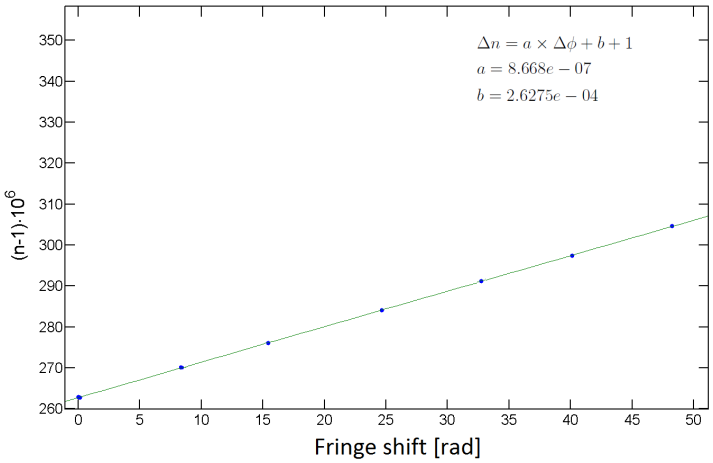

Figure 28: Calibration curve for the relation between fringe shift and the refractive index.

Red dashed lines show the change in refractive index calculated using fringe position measurements. It shows a strong correlation with the theoretical results shown in black. Figure inset shows the effect of measurement errors for HC-PBF length and refractometer pressure on the resolution of the refractive index measurement. The calibration plot is shown in Fig. 28. It was extracted from the measurement results and shows a linear relationship between fringe shift and the calculated refractive index change.

The fitting parameters a and b in the inset of Fig. 28 represent $\frac{\lambda}{2\pi L}$ and the refractive index of air for the wavelength, respectively in Eq.(32). The calibration measurement was carried out at the beginning of the study on the refractometer scheme that was rebuilt based on the design proposed by Igor Shavrin *et al.*. However, the calibration was not repeated after modifying the scheme to include two chambers. Because the length of HC-PBF had to be reduced for the new scheme, the calibration results presented here do not apply for the gas refractometer design developed in this study. This has an effect on the accuracy of the real refractive index measurement of acetylene gas. The absorption coefficient measurement depends only on the amplitude of the interference fringes, and not on the phase change. Thereby, the error in calibration has no effect on the measurement of the imaginary part of the complex refractive index of acetylene.

4.2 Complex refractive index of acetylene

The fringe response to light scanned over the resonance frequencies of acetylene were observed. An initial measurement was carried out at a low chamber pressure of ∼500 Pa to learn the fringe response to intrinsic refractometer properties. The dispersion properties of the SMF and the HC-PBF along with absorption at fibers' core walls was important to consider in order to accurately measure the refractive index of acetylene. In addition, the measurement at the low chamber pressure was used as reference to calculate the complex refractive index of acetylene, as explained in Section 3.2. The amplitude and phase response of the refractometer are shown in Fig. 29.

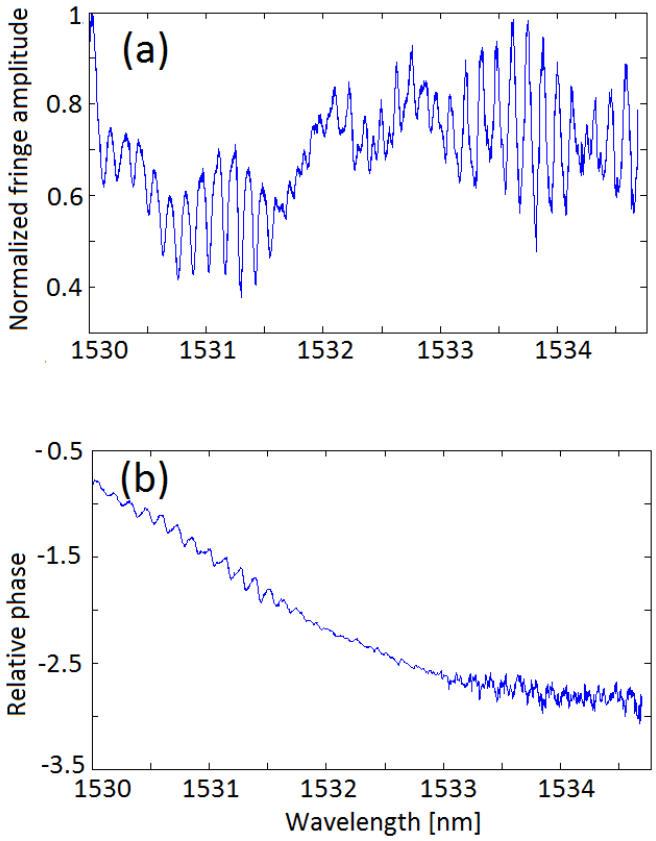

Figure 29: (a) Extracted normalized fringe amplitude and (b) phase (b) as a function of wavelength of light without acetylene at 500 Pa chamber air pressure. Wavelength scan in steps of 1 pm.

The phase response was almost flat from 1531.75 nm to 1532.9 nm in Fig. 29 (b). However, the amplitude change was detected. This could be due to high absorption at those wavelengths which made the detection of fringe movement difficult during analysis, even though the fringes were visible.

The wavelength of the tunable laser was scanned over the wavelength range from 1525 nm to 1545 nm where the P branch of the $\upsilon_1 + \upsilon_3$ band gives rise to a number of pronounced resonances for acetylene [13]. A 12.9 cm long HC-PBF was filled with acetylene using the setup described in Chapter 3. The acetylene pressure inside the chambers was measured to be equal 12 kPa. This volume of gas was experimentally found to be optimal to provide a clear reading of fringes by the CCD camera. Absorption of light at measurement wavelengths by acetylene was too high at higher pressures for clear detection. For the first measurement, the tunable laser was set to a wavelength step of 5 pm. Figure 30 presents the the absorption spectrum and the change in refractive index.

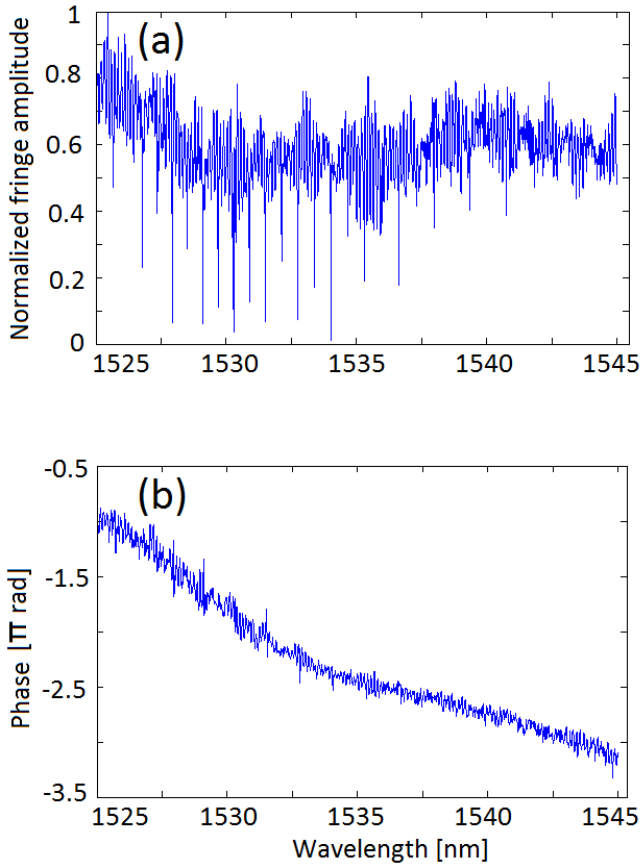

Figure 30: (a) Extracted normalized fringe amplitude and (b) fringe position as a function of wavelength with 96% pure acetylene. Wavelength scan was performed in steps of 5 pm.

The measurement was performed with 5 pm wavelength steps. This revealed a number of resonance frequencies of acetylene in the wavelength range from 1530 nm to 1534 nm. The relation between absorption coefficient and the refractive index change at resonance frequencies was difficult to detect during this measurement.

The wavelength step was found to be too large to observe the phase change clearly in Fig. 30(b). To obtain a better fringe response at the resonance frequencies of acetylene, the measurement was repeated with a wavelength step of 1 pm over the 1530 nm to 1534 nm wavelength range. The results of the measurement are shown in Fig. 31.

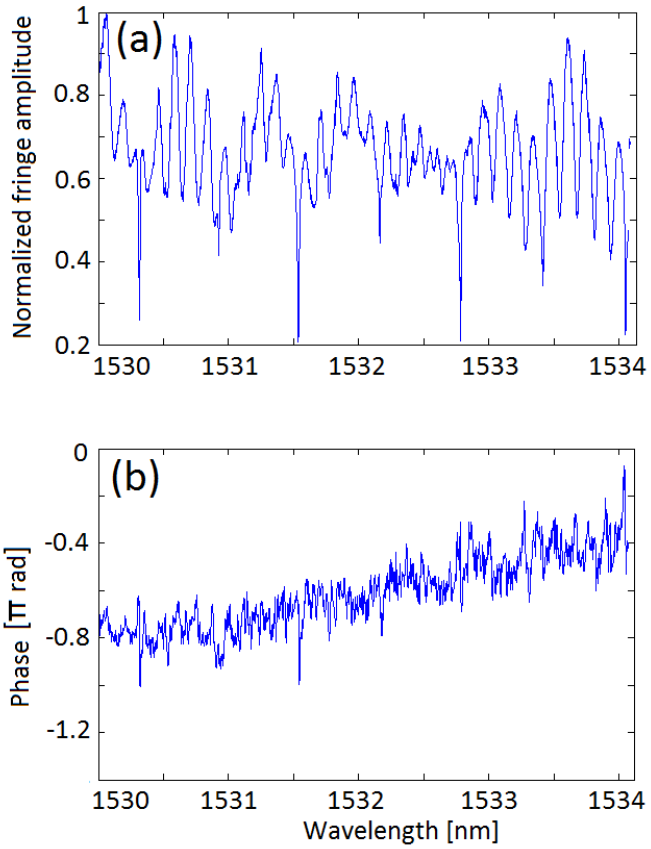

Figure 31: (a) Extracted normalized fringe amplitude and (b) fringe position as a function of wavelength with 96% pure acetylene. Wavelength scan was performed in steps of 1 pm.

The absorption spectrum for acetylene over the wavelength range is resolved in this measurement. The corresponding change in refractive index at those wavelengths can be seen as the phase change in Fig. 31 (b). The absorption coefficient and refractive index were calculated for these measurement results.

The measurements performed for ∼500 Pa air was used as reference to calculate the complex refractive index of acetylene. The absorption coefficient for acetylene was calculated for the wavelengths that showed the highest resonant response using formulas (37) and (38). The length of the sample fiber L_s was 12.9 cm. The result is shown in Fig. 32.

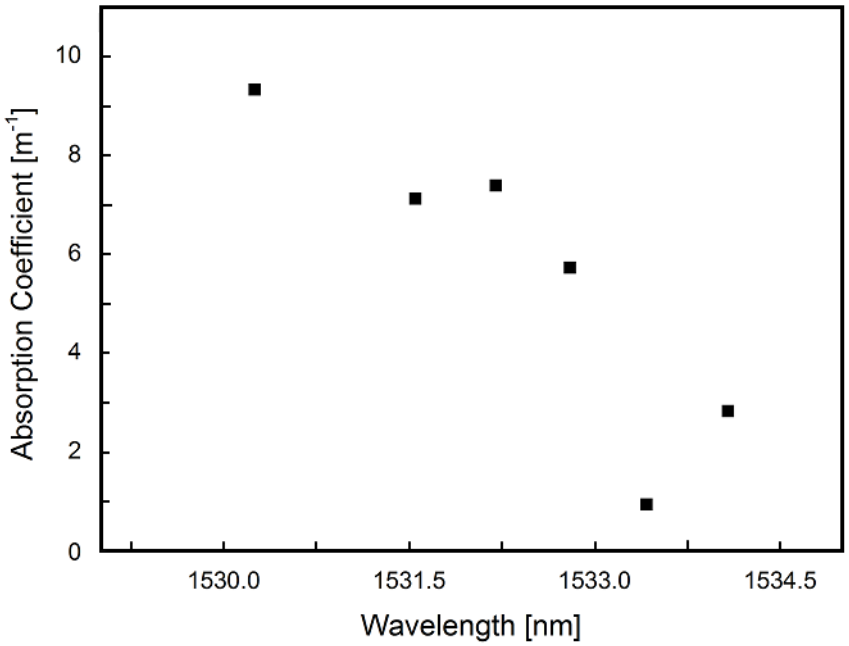

Figure 32: Determination of the absorption coefficient as a function of wavelength for ∼96% pure acetylene gas.

In order to calculate the real refractive index of acetylene, the difference in phase between the air measurement and the acetylene measurement were taken. As shown in Eq. (31), the phase difference between the two measurements is related to the refractive index of air, which is known, and the refractive index of acetylene. However, phase change measurement for air were not clear, as can be seen in Fig. 29(b). The measurements at 1533.3 nm and 1534 nm wavelengths were taken for both air and acetylene, and the refractive index of acetylene at those wavelengths were calculated using Eq. (32). The difference between the two measurements were used to determine the resolution of the refractometer, which is the smallest change in refractive index that the refractometer can detect. This was found to be 2×10^{-7} RIU.

5 Discussion

The gas refractometer device built during this thesis enabled us to measure the complete complex refractive index of 96% pure acetylene gas within the optical C-band. The spectral behavior of the refractive index of acetylene around 1530 nm to 1534 nm were observed. The absorption coefficients at the resonance frequencies were calculated. The resolution of the refractometer was determined by calculating the smallest refractive index change that the device could detect.

For this study, the refractometer design proposed by Igor Shavrin *et al.* [12] was modified. In their paper, the optimum acetylene concentration in the HC-PBF that could be measured was 14%. The aim of this thesis was to improve on their design to enable the measurement of pure acetylene gas. The refractometer scheme developed here can, in principle, measure the complete complex refractive index of pure acetylene. However, it was not possible to maintain a high vacuum environment in the refractometer due to leaks in the tubes that were used to connect the chambers. Some of the connectors that were employed to clamp the tubes and secure them to the chambers were made from plastic. They are not suitable in a high vacuum system, which caused ambient air to leak into the system. These could not be fixed within the time frame of the experimental work. In addition, the type of vacuum pump employed was not suitable to evacuate air completely before introducing acetylene into the refractometer. The measurements were conducted with acetylene mixed with ∼500 Pa of air, which resulted in ∼96% pure acetylene. It was possible to maintain both ends of the HC-PBF at chamber pressure due to modifications introduced to the refractometer design. This allowed for equal pressure gradient of acetylene along the HC-PBF for efficient light-acetylene overlap.

The change in refractive index caused by the addition of acetylene induces a movement in the interference fringes at the output of the refractometer. When a wavelength scan is performed, the change in position of the fringes relates to the phase difference at that wavelength. The change in fringe amplitude relates to the absorption coefficient. For the first measurement, the refractometer had ∼500 Pa air, which was used as a reference as its refractive index is known. The laser was scanned over 1530 nm - 1534 nm and the amplitude and phase values were extracted. In the second measurement, the amplitude and phase values for ∼96% acetylene were extracted for the same wavelengths. The absorption coefficient of acetylene at those wavelengths were calculated using Eq.(37) and Eq.(38). In order to calculate the real refractive index of acetylene, the phase values over the scanned wavelengths for air and acetylene were used in Eq.(32). Our phase measurements for air were imprecise, and the refractive index of acetylene could only be measured at two wavelengths. The difference in refractive index at those wavelengths were used to estimate the resolution of the device.

The linear relationship between a change in the real refractive index and the movement of fringes was established in the calibration measurement in Fig. 28. However, the

calibration was carried out at the beginning of the experimental work using a HC-PBF of length that was different from the one used for the complex refractive index measurement. This affected the accuracy of the final measurement of the refractive index. The absorption coefficient calculation only depends on the amplitude of the fringes, and not the change in the fringe position with the change in refractive index. The incorrect calibration of the instrument did not affect the absorption coefficient results.

The Mach-Zehnder-type design of the refractometer is simple to implement yet accurate. The equal pressure gradient of acetylene gas along the sample fiber should, in principle, improve the device resolution as it leads to a better overlap between the gas and light. However, alterations to the length of the HC-PBF that were required to accommodate it on the V-groove inside the new chamber introduced uncertainties with regard to its length. In addition, the coupling efficiency between SMF1 and HC-PBF was low - $\sim$10% of the light from SMF1 was coupled into the HC-PBF. This reduced the intensity of the interference fringes at the output, and made it difficult for the analysis program to pick up the fringes from the camera images. The design can be improved by replacing the V-groove with a more efficient coupling mechanism, and having the length of the HC-PBF as a fixed parameter from the start. The intrinsic property of HC-PBF also leads to modal interference (MI). At short fiber lengths (0.1 - 10 m) the HC-PBF can support surface modes at the core-cladding interface and cladding modes in addition to core modes. The excitation of additional modes besides the lowest order core mode results in modal interference effects. Time dependent background modulation is produced that limits the device sensitivity to absorption lines of a gas [49]. MI effects are more significant at short lengths as all additional modes that are excited inside the HC-PBF have high differential loss. The influence of MI on the accuracy of the refractometer can be reduced by increasing the length of the HC-PBF.

Refractive index of pure acetylene has been measured before with a resolution of 6.6×10^{-8} using a fiber based Fabry-Perot-type refractometer [50]. Fiber optic gas sensor that can detect acetylene gas based on absorption spectroscopy have also been demonstrated [51]. However, the fiber-optic sensor design proposed in this thesis is capable of measuring the refractive index and absorption coefficient of $\sim$96% pure acetylene gas simultaneously. Despite the reduced accuracy of the device, the refractometer was capable of measuring the complete complex refractive index of $\sim$96% pure acetylene. The utilization of a HC-PBF as a sample waveguide required very little volume of acetylene gas for sensing, and allowed for a long interaction length. In addition, the fiber based design makes it possible for the refractometer to be made compact and suitable for in-situ measurement. This has important implications especially in chemical sensing.

6 Conclusion

In this thesis, a fiber-optic refractometer based on Mach-Zehnder-type interferometer with a HC-PBF as a sample cell and waveguide was experimentally studied. The refractometer design proposed by Igor Shavrin *et al.* was modified in an attempt to measure the complete complex refractive index of pure acetylene. The modification enabled the measurement of ∼96% pure acetylene, while maintaining a uniform gas pressure along the entire HC-PBF.
Acetylene gas was introduced into the refractometer at 12 kPa total pressure. The gas diffused into the hollow core of the HC-PBF uniformly which changed the effective refractive index of the fiber. The real refractive index of acetylene was calculated by measuring the change in fringe position at the output of the refractometer. Similarly, the absorption coefficient was calculated by observing the change in fringe amplitude. A good fringe response at the resonance frequencies of acetylene required only a small volume of acetylene gas. This is an important feature of the refractometer that adds to the safety of the design when testing volatile gases.

Many of the proposed gas refractometer devices promise good sensitivity and resolution, but only provide the real or the imaginary part of the complex refractive index. The refractometer proposed by Igor Shavrin *et al.* was the first proof-of-principle experimental implementation of a fiber-optic Mach-Zehnder-type interferometer capable of measuring the complete complex refractive index of acetylene gas simultaneously. However, the design required one end of the HC-PBF to be exposed to ambient pressure. This resulted in an unequal pressure gradient of analyte gas along the fiber. Pure acetylene is also highly absorbent at atmospheric pressure, so an air-acetylene mixture was used as the analyte. These issues were dealt with by the modifications to the refractometer design introduced in this thesis. The absorption spectrum of ∼96% pure acetylene in the P-branch of the $\upsilon_1 + \upsilon_3$ was measured. The refractometer scheme studied provided a refractive index resolution of 2×10^{-7} RIU.

The resolution of the refractometer was affected by the uncertainty in fibers' lengths and modal interference in the HC-PBF. The addition of the V-groove system to couple light into the HC-PBF added to the difficulty in accurately measuring the length of the sample arm of the refractometer. In addition, high coupling loss was detected between the SMF and HC-PBF in the V-groove system. These factors affected the final measurement resolution.

References

[1] *Abbe Refractometer*, Humboldt State University, http://www2.humboldt.edu/scimus/RefracExhibit/AbbeDesc/ZeissAbbe1893.htm

[2] J.V. Hughes, *A new precision refractometer*, Journal of Scientific Instruments **18**, 234-237 (1941).

[3] S. D. Woodruff and E. S. Yeung, *Double-beam Fabry-perot interferometry as a refractive index detector in liquid chromatography*, Analytical Chemistry **54**, 2124-2125 (1982).

[4] G. Coppola, P. Ferraro, M. Iodice, and S. D. Nicola, *Method for measuring the refractive index and thickness of transparent plates with lateral-shear, wavelength-scanning interferometer*, Applied Optics **42**, 3882-3887 (2003).

[5] H. Shao, W. Wang, S. E. Lana, and K. L. Lear, *Optofluidic intracavity spectroscopy of canine lymphoma and lymphocytes*, Photonic Technology Letters **20**, 493-495 (2008).

[6] S. R. Kachiraju and D. A. Gregory, *Determining the refractive index of liquids using a modified Michelson interferometer*, Optics & Laser Technology **44**, 2361-2365 (2012).

[7] J. M. Starnaud, J. Ge, J. Orbriot, T. K. Bose, and P. Marteau, *An accurate method for refractive index measurements of liquids using two Michelson laser interferometers*, Review of Scientific Instruments **62**, 1441 (1991).

[8] J. J. Fendley, *Measurement of refractive index using Michelson interferometer*, Physics Education **17**, 209 (1982).

[9] T. Schubert, N. Haase, H. Kuck, and R. Gottfried-Gottfried, *Refractive index measurements using an integrated Mach-Zehnder interferometer*, Sensors and Actuators A **60**, 108-112 (1997).

[10] H. Tai, H. Tanaka, and T. Yoshino, *Fiber-optic evanescent-wave methane-gas sensor using optical absorption for the 3.392-Mu m line of a He - Ne laser*, Optics Letters **12**, 437-439 (1987).

[11] C. Ming-Hung, H. Shao-Nan, and Y. Hsiharng, *D-type fiber optic sensor used as a refractometer based on total-internal reflection heterodyne interferometry* **101**, 322–327 (2004).

[12] I. Shavrin, S. Novotny, A. Shevchenko, and H. Ludvigsen, *Gas refractometry using hollow-core photonic bandgap fiber in a Mach-Zehnder-type interferometer*, Applied Physics Letters **100**, 051106 (2012).

[13] T. Ritari, J. Tuominen, J. C. Petersen, T. Sørensen, T. P. Hansen, H. R. Simonsen, and H. Ludvigsen, *Gas sensing using air-guiding photonic bandgap fibers*, Optics Express **12**, 4080 (2004).

[14] *TIE-29: Refractive Index and Dispersion* Technical Information, Advanced Optics (2007).

[15] W. D. Nicholas, *Determination of temperature and composition dependence of refractive index in binary solutions* (Master's thesis) Clarkson University (2011).

[16] Q. Hang, *All photonic bandgap Bragg fiber refractometers* (Doctoral dissertation), University of Montreal (2013).

[17] J. Rheims, J. Köser, and T. Wriedt, *Refractive index measurements in the near-IR using an Abbe refractometer* Measurement Science and Technology **8**, 601-605 (1997).

[18] P. Cecile, *ABBE Zeiss Refractometer*, Louisiana State Universiy, http://macro.lsu.edu/HowTo/Abbe_refractometer.pdf.

[19] Y. Junwei, *et al.*, *Expanding the measurement range of a critical-angle refractometer through Fourier analysis*, Europhysics Letters **104**, 20001 (2013).

[20] T. Allsop, R. Reeves, D. J. Webb, and I. Bennion, *A high sensitivity refractometer based upon a long period grating Mach-Zehnder interferometer*, Review of Scientific Instruments **73**, 1702 (2002).

[21] Y. Jian, X. Chang-Qing, L. Yingfu, D. B. John, and Z. Mohammed, *Fringe spacing controllable long-period grating assisted Michelson interferometer for high sensitivity refractometry*, Proc./SPIE 7099, Photonics North 2008, 70992A (2008).

[22] I. R. Kenyon, *The Light Fantastic* (Oxford University Press 2008).

[23] J. P. Parry, B. C. Griffiths, N. Gayraud, E. D. McNaghten, A. M. Parkes, W. N. MacPherson, and D. P. Hand, *Towards practical gas sensing with micro-structured fibres*, Measurement Science and Technology **20**, 075301 (2009).

[24] C. H. Lee *et al.*, *Characteristics of a fiber Bragg grating temperature sensor using the thermal strain of an external tube*, Journal of the Korean Physical Society **59**, 3188-3191 (2011).

[25] H. Wen *et al.*, *Slow-light fiber-Bragg-grating strain sensor with a 280-femtostrain/Hz resolution*, Journal of Lightwave Technology **31**, 1804-1808 (2013).

[26] T. Horiguchi, T. Kurashima, and M. Tateda, *A technique to measure distributed strain in optical fibers*, Photonics Technology Letters **2**, 352-354 (1990).

[27] T. Kurashima, T. Horiguchi, and M. Tateda, *Distributed-temperature sensing using stimulated Brillouin scattering in optical silica fibers*, Optics Letters **15**, 1038–1040 (1990).

[28] A. Messica, A. Greenstein, and A. Katzir, *Theory of fiber-optic, evanescent-wave spectroscopy and sensors*, Applied Optics **35**, 2274-2284 (1996).

[29] J. P. Conzen, J. Bürck, and H. J. Ache, *Characterization of fiber-optic evanescent wave absorbance Sensor for nonpolar organic compounds*, Society for Applied Spectroscopy **47**, 753-763 (1993).

[30] B. D. Mac Craith, C. Mcdonagh, G. O'Keeffe, T. Butler, B. O'Kelly, and J. F. Mcgilp, *Fibre optic chemical sensors based on evanescent wave interactions in sol-gel-derived porous coatings*, Journal of Sol-Gel Science and Technology **2**, 661-665 (1994).

[31] Z. Zhi-guo, Z. Fang-di, Z. Min, Y. Pei-da, *Gas sensing properties of index-guided PCF with air-core*, Optics and Laser Technology **40**, 167–174 (2008).

[32] J. D. Joannopoulus, S. G. Johnson, J. N. Winn, and R. D. Meade, *Photonic Crystals: Molding the Flow of Light* (second edition Princeton University Press 2007)

[33] F. Benabid, *Hollow-core photonic bandgap fibre: new light guidance for new science and technology*, Philosophical Transactions of the Royal Society A doi:10.1098/rsta.2006.1908.

[34] P. Russell, *Photonic crystal fibers*, Science **299**, 358–362 (2003).

[35] T. A. Birks, P. J. Roberts, P. S. Russell, D. M. Atkin, and T. J. Shepherd, *Full 2-D photonic bandgaps in silica/air structures*, Electronics Letters **31**, 1941–1943 (1995).

[36] P. S. Russell, *Photonic band-gaps*, Physics World **5**, 37–42 (1992).

[37] W. Jin, H. F. Xuan, and H. L. Ho, *Sensing with hollow-core photonic bandgap fibers*, Measurement Science and Technology **21**, 094014 (2010).

[38] H. K. Kim, V. Dangui, M. Digonnet, and G. Kino, *Fiber-optic gyroscope using an air-core photonic-bandgap fiber*, Proc. SPIE 5855, 17th International Conference on Optical Fibre Sensors, 198 (2005).

[39] P. J. Roberts *et al.*, *Ultimate low loss of hollow-core photonic crystal fibres*, Optics Express **13**, 236 (2005).

[40] M. S. Meyer and G. L. Eesley, *Optical fiber refractometer*, Review of Scientific Instruments **58**, 2047-2048 (1987).

[41] C. Minh, L. Guillaume, D. Veronique, and F. Pierre, *Tilted fiber Bragg grating photowritten in microstructured optical fiber for improved refractive index measurement*, Optics Express **14** 10359-10370 (2006).

[42] Y. L. Hoo, W. Jin, H. L. Ho, D. N. Wang, and R. S. Windeler, *Evanescent-wave gas sensing using microstructure fiber*, Optical Engineering **41**, 8–9 (2002).

[43] J. Michael Hollas, *Modern Spectroscopy* (Fourth edition Wiley 2004).

[44] I. Shavrin, *Refractometer model (Special assignment)*, Fiber optics group, Aalto University (2012).

[45] B. E. A. Saleh and M. C. Teich, *Fundamentals of Photonics* (Second edition Wiley 2007).

[46] K. P. Birch and M. J. Downs, *An updated Edlén equation for the refractive index of air*, Metrologia **30**, 155-162 (1993).

[47] K. P. Birch and M. J. Downs, *Correction to the Updated Edlén equation for the refractive index of air*, Metrologia **31**, 315-316 (1994).

[48] *Tunics-PR/PRI wavelength tunable laser diode source*, User's guide, http://www.equipland.com/objects/catalog/product/extras/1520_Photonetics_Tunics_PR_PRI_Manual.pdf

[49] M. N. Petrovich, F. Poletti, and D. J. Richardson, *Analysis of modal interference in photonic bandgap fibers*, Transparent Optical Networks (ICTON), 1-4 (2010).

[50] F. Xu, L. Lu, W. Lu, and B. Yu, *In-line Fabry-Perot refractive index sensor based on microcavity*, Chinese Optics Letters **11**, 1-4 (2013).

[51] G. Yan, A. P. Zhang, G. Ma, B. Wang, B. Kim, J. Im, S. He, and Y. Chung, *Fiber optic acetylene gas sensor based on microstructured optical fiber Bragg gratings*, IEEE Photonics Technology Letters **23**, 1588-1590 (2011).